

Amundsen Sea Ice Production and Transport

Karen M. Assmann and Hartmut H. Hellmer

Alfred Wegener Institute for Polar and Marine Research, Bremerhaven, Germany

Stanley S. Jacobs

Lamont-Doherty Earth Observatory of Columbia University, Palisades, U.S.A.

Submitted 01/11/2004

Revised version submitted 30/3/2005

Corresponding author address:

K. M. Assmann, Alfred Wegener Institute for Polar and Marine Research,
Bussestr. 24, D-27570 Bremerhaven, Germany.

now at: Bjerknes Centre for Climate Research, c/o Geophysical Institute, University
of Bergen, Allégaten 70, N-5007 Bergen, Norway.

(e-mail: Karen.Assmann@bjerknes.uib.no)

Abstract. The drift and variability of sea ice in the Amundsen Sea are investigated with ice buoys deployed in March, 2000, and a coupled ice-ocean model. The BRIOS model results are compared with *in situ* ocean, atmosphere and sea ice measurements, satellite sea ice observations, and 8-19 months of buoy drift data. We identify a zone of coastal westward drift and a band of faster eastward drift, separated by a broad transition region characterized by variable ice motions. The model represents drift events at scales approaching its resolution well, but is limited at smaller scales and by deficiencies in the NCEP forcing. Two-thirds of the modelled sea ice production in the southern Amundsen moves westward near the coast, its transport modulated by meridional wind strength, damping sea ice formation in the eastern Ross Sea. One half of the ice exported from the Ross moves eastward into the northern Amundsen Sea, a net sea ice sink that also receives more than one third of the ice generated to its south. A low rate of exchange occurs with the Bellingshausen Sea, which must have a more independent ice regime. Snow ice formation resulting from high precipitation accounts for one quarter of the ice volume in the Amundsen Sea aiding the formation of a thick ice cover in a region with generally divergent ice drift. Freshwater extraction by sea ice formation is roughly balanced by precipitation and ice shelf melting, but a positive trend in the surface flux is consistent with an Amundsen source for a reported freshening in the Ross Sea.

Keywords:

numerical modelling, sea ice drift, Southern Ocean, interannual variability, freshwater flux

1. Introduction

January 30, 1774. “The outer or Northern edge of this immense ice field was composed of loose or broken ice so closely packed together that nothing could enter it; about a Mile in began the firm ice, in one compact solid boddy, and seemed to increase in height as you traced it to the South; In this field we counted Ninety Seven Ice Hills or Mountains, many of them vastly large we could not proceed one Inch farther South being at that time in the Latitude of $71^{\circ} 10'$ South, Longitude $106^{\circ} 54'W$ ”.

Those words recorded the southernmost position achieved by the *Resolution* on James Cook’s pioneering voyages in the Southern Ocean (Jones 1982). 65 years later the U.S. Exploring Expedition’s William Walker was dispatched to try and better Cook’s high latitude record. His schooner, the *Flying Fish*, while setting a record for its own expedition, only reached $\sim 70^{\circ} 14' S$, $101^{\circ} 11' W$ on 22 March 1839 (Philbrick 2003). Immense ‘ice islands’ were again encountered, along with ‘ice stretching in all directions as far as the eye could reach.’

Persistent summer sea ice in the Amundsen Sea has historically made it one of the worst sectors to try and reach the white continent. That ice continues to frustrate mariners to the present day, in spite of the availability of modern ice-breakers. But the Amundsen continental shelf has been pen-

Copyright 2005 by the American Geophysical Union.

Paper number .

0148-0227/05/\$9.00

etrated several times since 1990, usually in heavy pack and around numerous icebergs, revealing ocean characteristics intermediate between the Bellingshausen and the Ross Seas. Circumpolar Deep Water (CDW) dominates the deep circulation on the eastern shelf, along with the upwelling beneath and seaward of ice shelves and floating glaciers (Hellmer et al. 1998). In combination with the nearly perennial ice cover these circulations are believed to preclude most dense shelf and bottom water production.

Renewed interest in the Amundsen Sea has followed from observations of sea ice retreat (Jacobs and Comiso 1997) and reports of strong melting under the Pine Island Glacier (Jenkins et al. 1997). The ocean may play a key role in the mass balance of the West Antarctic Ice Sheet, and an improved understanding of the ice-ocean interaction and ocean circulation is needed in this region (Jenkins et al. 1997). Recent work has linked the variability of the Antarctic sea ice extent with lower latitude phenomena (Yuan and Martinson 2000). Hereby, the Amundsen, and Bellingshausen Seas were identified as those regions where the lower-latitude signal enters the Southern Ocean. It has also been postulated that freshening in the Ross Sea over recent decades may reflect increased melting and/or decreased sea ice production upstream in the Amundsen and Bellingshausen sector (Jacobs et al. 2002).

Here we use a coupled ice-ocean model, forced by NCEP reanalysis atmosphere data, to investigate the formation and transport of sea ice in the Amundsen Sea (100-150°W). After a model description, we compare the NCEP forcing data to limited atmospheric observations in the region, and use SSM/I data, sea ice observations and ocean measurements from the *Nathaniel B. Palmer* (Giulivi and Jacobs 1997) to validate ice extent, thickness and water mass characteristics. Following a description of the modelled mean sea ice drift, thickness and growth, the simulated sea ice drift is compared to the tracks of three sea ice drift buoys. The buoys were deployed in the eastern Amundsen Sea in late March 2000, supplied data for periods between 8 and 19 months and drifted through the region from 105°W to 140°W (Fig. 1 and Table 1). Drifter A-1 was set close to the position where the Resolution reached its highest southern latitude. Finally, we analyse the sea ice transport and freshwater budget of the Amundsen Sea and its interannual variability.

2. Model

2.1. Model Description

The coupled ice-ocean model BRIOS2.2 (Bremerhaven Regional Ice Ocean Simulations) employed here has been previously applied to the Ross and Weddell Seas (Timmermann et al. 2002 a, b, Assmann et al. 2003, Assmann and Timmermann 2005). The ocean component is based on the S-coordinate Primitive Equation Model SPEM (Haidvogel et al. 1991), and the sea ice component on a dynamic-thermodynamic sea ice model with viscous-plastic rheology (Hibler 1979). Parkinson and Washington (1979) thermodynamics are employed, using the Semtner (1976) zero-layer approach for heat conduction. Inclusion of a prognostic

snow layer (Owens and Lemke 1990) accounts for the effect of flooding (Leppäranta 1983; Fischer 1995). Interactions between ice shelf base and ocean are treated the same as between sea ice and ocean, whereby the freezing point temperature is calculated as a function of pressure and salinity for the whole model domain (Timmermann et al. 2002 a).

Ice shelf and water column thicknesses for the Ross Ice Shelf cavity are from Greischar et al. (1992) and ice thickness is set constant to 200 m for the smaller ice shelves, Abbot (72.5° S, 95° W) and Getz (74° S, 125° W), in and east of the Amundsen Sea. The model is run on a circum-polar grid with zonal boundaries at 50° S and 82° S, has an isotropic resolution of 1.5° zonally and 1.5° cos(ϕ) meridionally for the whole domain, and 24 vertical levels with increasing resolution near surface and sea floor. Bottom topography is from Smith and Sandwell (1997) north of 70° S, and ETOPO5 data south of 70° S. The hydrographic data for initialization and boundary restoring are from the WOCE Hydrographic Programme Special Analysis Centre (Gouretski and Jancke 1998).

2.2. Model Forcing

For atmospheric forcing, daily NCEP Reanalyses for the 10-m wind velocities, 2-m air temperature, specific humidity, cloudiness, and precipitation (P-E) were used from 1958-1977 to spin-up the model and from 1978-2001 for analysis. Prior to 1978, the NCEP Reanalyses do not include satellite data and are believed to be of lesser quality (Tennant 2004).

During February and March 2000 NCEP winds were compared to daily mean shipboard measurements from *N.B. Palmer* cruise NBP00-01 in the study area (Fig. 2). Average wind speed and direction at the ship's mean position each day yielded values for 27 days between 20 Feb 2000 and 23 Mar 2000. These were compared to the NCEP wind data at the closest model grid point. Wind directions were more often southwest and southeast (Fig. 2) in an area commonly assumed to be dominated by easterlies. While the correlation between NCEP and shipboard wind time series is weak ($r=0.33$ for magnitude and $r=0.37$ for direction), the general agreement between shipboard and NCEP directions and speed maxima show that the NCEP fields are tracking atmospheric lows within a day or two. Lower NCEP wind speeds for the first half of the record may indicate an underestimation of strong synoptic systems or katabatic winds near the coastline where the ship frequently worked. While our comparison only covers a short period, high winds are known to be underestimated by the NCEP Reanalyses (Cullather et al. (1997), Smith et al. (2001), and Yuan 2004). Daily NCEP wind speeds averaging 1.4 m s⁻¹ less than the observations may be a source of model error, although a standard deviation of 3.95 m s⁻¹ on their mean difference is not indicative of a systematic offset.

Air temperature records obtained from the sea ice drift buoys were used to evaluate the quality of the NCEP air temperatures in the Amundsen Sea. The comparison of observed and NCEP air temperatures along the track of buoy A-3, which covers more than a full seasonal cycle from March 2000 to October 2001 (Fig. 1 and Table 1), indicates that

NCEP temperatures are higher with an average of 3°C from mid-October to February (Fig.3). This induces an early onset of the melting period and a late start of sea ice growth in the model. By contrast, NCEP winter air temperatures are on average $5\text{-}6^{\circ}\text{C}$ colder than those observed, likely due to a stronger continental influence resulting from the 210 km meridional resolution as suggested from a comparison of the NCEP and real coastlines. Both time series show a large range and high-frequency variability reflecting the passage of low-pressure systems. Since air temperatures are well below the ocean surface freezing point throughout winter, when the sea surface is insulated from the atmosphere by a nearly closed ice cover, these have a minor effect on sea ice production or decay. Assmann and Timmermann (2005) investigated sea ice formation in the Ross Sea and found sea ice growth to be independent of air temperatures during winter. The comparison of observed and NCEP air temperatures along the tracks of the other two buoys, both of which yielded data from March to November 2000 show the same pattern of temperature differences before and after mid-October. To evaluate the model sensitivity to the summer overestimation of NCEP air temperatures a sensitivity experiment was performed in which an upper limit of -1.9°C was imposed on air temperatures in sea ice covered grid boxes (in the following referred to as T_FREEZE).

2.3. Evaluation of model performance

2.3.1. Sea Ice Concentration and Extent.

We compared modelled sea ice extent and concentration with satellite SMMR and SSM/I data, using the bootstrap algorithm (Comiso 1999). In the reference simulation, August to December ice extents are nearly identical with the satellite data, but the January to July extents are substantially lower, with February ice extent underestimated by 60 % (Fig. 4 a). Restricting air temperatures in ice-covered grid boxes to below the freezing point reduces the underestimate to 35 %. High summer air temperatures in the NCEP Reanalyses thus negatively bias the model summer sea ice cover. An additional reason for this may lie in the absence of small scale events of high winds in the NCEP forcing which may reduce a dynamic increase of the ice thickness.

The ocean model may also lower the simulated summer sea ice extent. A model resolution too coarse to represent the continental shelf bathymetry in detail allows 'warm' circumpolar water masses to protrude further south than in reality enhancing sea ice melting. This process could be abetted or damped if the fresh water input from precipitation or ice shelf basal melting was too low or too high (Hellmer 2004).

Comparison of monthly and mean annual anomalies, i.e., monthly mean values with the mean seasonal cycle removed, shows that the model is able to reproduce the interannual variability of the sea ice extent (Fig. 4 b). The modelled variability is slightly larger than observed, but peak locations tend to correspond with those in the satellite data.

2.3.2. Sea Ice Thickness Distribution.

Observations of summer ice thicknesses were made along 135°W and 150°W in January 1999 (p.c., T. Tin and M. Jeffries, 2002) and compared with the modelled January mean

for 1999 and a 24-year January mean from 1978-2001 along the same longitudes (Fig. 5). As might be expected, the spatial variability in the observations is higher than that of the model results, even after smoothing due to different footprints.

The 1999 observations show greater sea ice thickness, on average 0.24 m (0.25 ± 0.55 m for 135°W , 0.22 ± 0.23 m for 150°W) above the modelled values for the reference experiment. This corresponds to an underestimation of 25% for 135°W (mean observed sea ice thickness 1.02 ± 0.94 m) and of 33 % for 150°W (0.60 ± 0.42 m). Limiting air temperatures to values below the sea surface freezing point over ice covered grid boxes overestimates sea ice thicknesses by 0.32 m for 135°W and 0.20 m for 150°W indicating that the chosen remedy overcompensates for the deficiencies of the NCEP forcing data. Also notable is a smooth northward decrease of sea ice thickness in the model results, whereas the observations in both sections show a distinct boundary at 72°S with a thicker ice cover (≥ 1 m) and large thickness variations south and a smoother ice pack with thicknesses ≤ 1 m north of this latitude (Fig. 5). The finite difference discretization scheme and the viscous-plastic rheology of the sea ice model treat the ice pack as a viscous fluid and thus induce some degree of smoothing.

Winter ice thicknesses were compared with data from a September-October 1994 cruise in the Amundsen and eastern Ross Seas between 110°W and 170°W , and $66\text{--}71^\circ\text{S}$ (Jeffries et al. 1998). With a mean observed ice thickness of 0.84 ± 0.46 m and mean modelled values of 0.97 ± 0.37 m (reference) and 0.99 ± 0.34 m (T_FREEZE), thicknesses agree within the uncertainties. The 24-year winter mean of 1.00 ± 0.32 m for both model experiments indicates that the limitation of air temperatures to below the sea surface freezing point only affects summer sea ice thicknesses. We conclude from these comparisons that the two simulations can be used as bounding values on sea ice transport.

2.3.3. Ocean Properties.

Observed water mass characteristics in the Amundsen Sea can be used to evaluate the ocean component of the model. Some of the end-of-summer (March) observations show surface waters (AASW) cooling toward the sea surface freezing point (Fig. 6a) above denser Winter Water (WW), the remnant of prior winter convection. Others indicate warmer waters, mostly from surface heating during the waning summer. Relatively warm ($> 1.5^\circ\text{C}$) and salty (~ 34.7) CDW underlies the surface waters and locally upwells near the coastline after substantial melting of ice shelf bases (Hellmer et al. 1998).

The water mass characteristics observed in the Amundsen Sea are generally reproduced by the model (Fig. 6b). Temperatures below the surface freezing point are found close to the modelled Abbot and Getz ice shelves, a region not covered by the observations. Its warmer CDW components (Fig. 6b) result from southward transport within the eastern branch of the Ross Gyre which occurs to the west of the cruise track which provided the data for Figure 6a.

On average, the modelled surface water (AASW) appears slightly warmer and fresher than observed, possibly due to

the overestimated sea ice melting in spring and summer. In the T_FREEZE experiment AASW salinities increased along with slightly colder temperatures as a result of the improved summer sea ice extent. However, a less desirable effect of the decreased sea ice melting is the formation of AASW and WW more saline than observed. This increases the shallow pycnocline strength between AASW and WW, causing the sea ice growth to increase by $\approx 25\%$ in T_FREEZE, but could also allow enhanced vertical heat flux from the CDW. While summer sea ice extent and thickness in the T_FREEZE experiment are closer to observations, the resulting changes in the surface freshwater balance lead to a less realistic stratification.

The modelled freshwater input from the Abbot and Getz Ice Shelves amounts to 85 Gt a^{-1} . This number is less than 60% of an earlier estimate for the whole Amundsen Sea (Jacobs et al. 1996), assuming that it occupies roughly half the SE Pacific sector. However, our model does not include other small ice shelves such as the rapidly melting Pine Island, estimated at 28 Gt a^{-1} by Jenkins et al. (1997), nor does it include meltwater from icebergs that calve and drift through the Amundsen Sea. The increase in mean net sea ice growth rate from the reference model experiment (395 Gt a^{-1}) to T_FREEZE (497 Gt a^{-1}) is 102 Gt a^{-1} . Considering that only part of the 85 Gt a^{-1} modelled glacial meltwater is advected into the Amundsen Sea, the additional glacial meltwater input from smaller ice shelves not included in the model would be sufficient to compensate for a large part of the surplus brine release in the T_FREEZE model experiment. Also, a more realistic freshwater input from ice shelves may lead to a stable water column and consequently to a thicker sea ice cover (Hellmer 2004).

3. Mean Modelled Sea Ice Drift Pattern

The large-scale modelled sea ice drift pattern in the Bellingshausen ($60\text{-}100^\circ\text{W}$), Amundsen ($100\text{-}150^\circ\text{W}$) and Ross Seas ($150^\circ\text{W}\text{-}160^\circ\text{E}$) is illustrated as a winter mean (May-October) in Figure 7. The most prominent features are a 5 cm s^{-1} westward drift within 100-300 km (3-7 grid cells) of the coastline and a larger zone of strong (up to 15 cm s^{-1}) eastward drift extending northward to the sea ice margin. These regimes are separated by a transition zone of low velocities ($1\text{-}2 \text{ cm s}^{-1}$) and variable direction that roughly follows the continental shelf break from the Antarctic Peninsula to about 115°W . The continental shelf then narrows westward to 150°W , while the transition from westward to eastward drift remains near 72°S into the eastern Ross Sea (165°W), reflecting the width of the easterly and the extent of the southerly wind influence.

The thickest ice appears along the coastline from $115\text{-}120^\circ\text{W}$ and $135\text{-}150^\circ\text{W}$, while the thinnest occurs near the outer ice edge. Both the thick and nearly stagnant regions of ice tend to coincide with the more persistent areas of summer sea ice (Gloersen et al. 1992). Most ice produced in the Bellingshausen is exported northward into the eastward flowing Antarctic Circumpolar Current (ACC), after initially moving westward like the *Belgica* in 1899 (Lecointe 1904). Ice generated in the southern Amundsen drifts west-

ward into the Ross Sea, where the drift pattern agrees well with that deduced from satellite observations (e.g., Drinkwater et al. 1999). These large scale drift characteristics are very similar to the pattern of NCEP surface winds (Fig. 8).

Predominant areas of freezing occur all along the coast (Fig. 8) where offshore winds generate narrow coastal leads and polynyas, some intermittent, but most only several kilometres wide and hence sub-grid scale. However, the model produces alternating convergent and divergent ice drift, due to the passage of low pressure systems, leading to areas of reduced ice concentration and high growth rates. Over the continental shelf, melting only occurs during summer (December to February), while in the eastward-drifting northern pack, where sea surface temperatures exceed the freezing point all year round, a broad band of melting is present even in winter. Sea ice in this region is only present due to advection and not due to local thermodynamic growth.

Earlier studies with the BRIOS model showed that a patch of net sea ice melting seaward of the Amundsen continental shelf (120-140°W) is due to upwelling of a westward travelling positive potential temperature anomaly that was present within the shelf break current throughout the 1980s (Assmann and Timmermann 2005). With a mean net annual growth rate of $1.50 \pm 0.24 \text{ m a}^{-1}$ for the area south of 70°S, the Ross Sea is the main formation site of sea ice in the Pacific sector. The Amundsen produces $0.69 \pm 0.30 \text{ m a}^{-1}$ south of the mean position of the drift transition, with the main area of sea ice growth east of 120°W. Zonal drift velocities of 4-5 cm s^{-1} in the coastal band imply a time of 13-16 months for sea ice formed in the eastern Amundsen Sea (110°W) to travel to the eastern Ross Sea (160°W). Consequently, multi-year sea ice found in the eastern Ross Sea is generally second year ice originating from the east.

4. Observed and modelled buoy drift

Three Alfred Wegener Institute (AWI) sea ice drift buoys with ARGOS identities 9358 (A-1), 9361 (A-2), and 9364 (A-3) were deployed on sea ice floes during late March 2000 on *Nathaniel B. Palmer* cruise NBP00-01 in the eastern Amundsen Sea (Fig. 1). All registered air temperature at 2-m height, air pressure at sea level, and position (GPS) for periods between 242 and 580 days (Table 1). Gaps towards the end of the drift of A-3 (Fig. 1, green and white broken lines) are caused by intermittent data transfer, perhaps as its ice floe decayed in rough seas. For analysis we will only use the continuous drift data up to 23 Oct 01.

The sea ice buoys all moved westward and slightly southward for most of their lifetimes, with short-term fluctuations superimposed on a general drift roughly parallel to the continental shelf break. Meridional fluctuations are largest for buoy A-1 and the first part of the drift of A-3 (A-3/1). These two northern buoys drifted within the transition from easterly to westerly winds (Fig. 7). They displayed a mean zonal drift speed of 2-3 cm s^{-1} , averaging 55 % of the more southerly drift of A-2 and A-3/2 within the band of coastal easterly winds (Table 1). In early August 2001, A-3 broke out of the pattern of zonal drift near 145°W, tracking north-

ward for several hundred kilometers before reversing zonal direction in the ACC (Fig. 1, green line). Intermittent A-3 buoy data after 23 Oct 01 indicate that meridional drift velocities of 6-8 cm s⁻¹ were attained.

Observed and modelled sea ice drift velocities were compared along the three buoy tracks. Figures 9 and 10 show the time series for both velocity components of buoy A-3, since it has the longest record, covering a full seasonal cycle and all of the drift regimes described above. All observed mean drift speeds fall in a fairly narrow range (10.0 - 14.5 cm s⁻¹) (Table 2), notable versus the mean u and v-components which vary strongly in magnitude, but in agreement with the mean NCEP wind speeds along the buoy tracks which lie between 453 and 510 cm s⁻¹. The model speeds display even narrower ranges of 8.8 - 9.5 cm s⁻¹ for the reference and 10.2 - 11.7 cm s⁻¹ for the T_FREEZE experiment. Drift speeds for the reference simulation average 20% lower than observed, likely due to the misrepresentation of strong synoptic systems in the NCEP data, and the resulting underestimation of wind speeds during high wind events (Fig.2, Yuan 2004). In the T_FREEZE experiment, which uses the same winds, speeds improve to a value of 5% below observations. Momentum transfer over large distances during the passage of strong synoptic systems and high winds will be enhanced by the more closed, thicker and rigid ice pack leading to faster drift.

A similar picture emerges when considering the root-mean-squares (rms) velocities of the u- and v-components (Table 3). For the u-component, rms velocities for the reference experiment are on average 85 % of the observations with a range from 72 % to 105%. The mean rms u-component for the T_FREEZE experiment is 101 % (78 % to 129 %) of the observed one. Modelled rms v-components only reach 71 % (66 % to 80 %) of the observed values for the reference and 84 % (79 % to 94%) for the T_FREEZE model experiment. The NCEP reanalyses are available on a 1.9°-grid in both latitude and longitude. This corresponds to a zonal resolution of ≈ 50 km at 75°S, but a meridional resolution of 210 km, an imbalance that can help to account for the larger v-component discrepancies.

For free ice drift, speeds are expected to be $\approx 2.5\%$ to 3% of the 10-m wind speed (Martinson and Wamser 1990, Fischer 1995). Along the buoy tracks values for the observations lie between 2.1 and 3.0%, for the reference simulation between 1.7 and 2.1% and for T_FREEZE between 2.1 and 2.4%. NCEP winds appear to be weaker than those observed and experienced by the buoys, and consequently the ratio of observed drift speeds to NCEP winds is likely to be slightly overestimated. Nonetheless, the modelled values suggest that the free drift assumption is largely applicable in the Amundsen Sea in winter, despite the large sea ice thicknesses and highly compact ice cover.

The model reproduces the general drift direction of 9 of the 12 drift components of the reference and of 10 out of 12 drift components of the T_FREEZE experiment (Table 2). Notable exceptions are the meridional drift of buoy A-3 and the zonal drift of buoy A-1 within the transition region between eastward to westward motion. This transition oc-

curs within a latitudinal band of 100-150 km, thus below the 210 km meridional resolution of the NCEP data. The eastward net zonal velocity of the simulated A-1, the low westward velocity for A-3/1, and the overestimated northward velocity of A-3/3 (Table 2) all suggest that the NCEP easterly-westerly transition is too far south leading to westerlies closer to the coast. The NCEP net zonal wind velocity for the buoy tracks within the transition region is westward, but small (Table 2). Nevertheless, the mean modelled winter position of the transition (Fig. 7) and the latitude band in which A-1 and A-3/1 drifted (Fig. 1) display good agreement. The model represents westward drift closer to the coast more accurately than near the drift transition, with zonal velocities between -3.7 (reference) and -4.7 cm s^{-1} (T_FREEZE). It should thus be feasible to obtain a realistic estimate of zonal sea ice transport from the Amundsen to the eastern Ross Sea.

The correlation coefficient between the observed and modelled time series average $r=0.72$ for the u-component and $r=0.64$ for the v-component for both model experiments, again with better agreement between the zonal velocities (Table 3). Smoothing the time series with a 5-day running mean to suppress variability at shorter time scales increases correlations between observed and modelled velocities to $r=0.84$ for the u-component and to $r=0.75$ for the v-component, corresponding to an average increase in variance explained of 19% (18% for T_FREEZE) for the u-component and of 15% (16% for T_FREEZE) for the v-component. Visual inspection of Figures 9 and 10 also shows that events at timescales longer than 5 days are generally well reproduced by the model. At drift speeds between $10\text{-}15 \text{ cm s}^{-1}$ the buoys cover a distance of $\sim 50 \text{ km}$, which corresponds to the model resolution in this area, within 5 days. Drift variability on shorter time scales thus takes place at the model's sub-grid scale making its representation difficult. In addition, any atmospheric variability on temporal and spatial scales below those of synoptic features is below the resolution of the NCEP forcing data. Their large-scale smoothed structure reduces the model's ability to reproduce extreme peak drift velocities (e.g. Fig. 9 at day 165 and 220).

Displayed as time series, velocity differences between model and observation are similar to the actual drift velocities, i.e., larger than a visual comparison of the timeseries, which shows reasonably well-matched peaks, might suggest (Fig. 9 and 10). This may be due to offsets of the order of one day in the passage of cyclones in the NCEP data, consistent with the earlier comparison between ship and NCEP wind directions. Differences between model and observation are largest for A-1 and A-3/1, within the transition zone where velocities are large and variable.

The relative influence of wind and ocean currents on sea ice drift was evaluated by a sensitivity study in which the sea ice was only driven by the wind (NO_OCEAN). Differences in drift velocity to the reference experiment are considerably smaller than those from comparisons with observations and with the T_FREEZE experiment, i.e., less than the differences caused by thermodynamic changes of the ice pack (Fig. 9 and 10). Changes in the net zonal and meridional

drift velocities are negligible ($\sim 0.1 \text{ cm s}^{-1}$) for A-2 and A-3/2 within the westward coastal drift, where modelled ocean surface currents are weak ($\sim 1.0 \text{ cm s}^{-1}$). An intensified coastal current only appears intermittently near the coastline in the southeast Amundsen Sea (Fig. 11). Continuous westward oceanic transport occurs only below 300 m depth in the form of a bottom-intensified shelf break current (Assmann & Timmermann 2005).

The lack of ocean influence does significantly influence net drift velocities for the A-1 and A-3/1 buoy tracks within the transition region between easterly and westerly winds. The modelled eastward ocean surface currents are consistent with the eastward drift of A-1 in the reference experiment and its small eastward translation in T_FREEZE (Fig.11). In the NO_OCEAN experiment, the westward drifts of A-1 and A-3/1 are small, but comparable to the ocean surface currents. The northward drift of A-3 near 145°W appears to be wind-driven, since the modelled ocean surface currents are directed southeastward in this region, following the eastern limb of the Ross Gyre (Fig.11).

5. Budgets & volume transports

Moving to larger temporal and spatial scales, we next quantify sea ice transport to and from the Amundsen Sea and consider the factors governing of its variability. Boundaries for the southern Amundsen Sea are set zonally at the coastline and the winter mean position of the west to east transition as shown in Figure 7, and meridionally at 100°W , and 150°W (Fig. 12). The latter differs from the 130°W used, e.g., by Gloersen et al. (1992), but encompasses the buoy tracks (Fig. 1) and most of the Amundsen continental shelf. Relevant quantities like sea ice volume, growth rates, and wind speed are calculated as means or sums over this $5.72 \times 10^5 \text{ km}^2$ area. North of the transition line the mean winter sea ice edge as indicated in Fig. 7 is used as a northern boundary, with eastern and western boundaries as defined for the southern part (Fig. 12).

The full Amundsen Sea sector experiences a net import of sea ice of $10.5 (11.0) \times 10^3 \text{ m}^3 \text{ s}^{-1}$ (number in brackets indicate transport values for the T_FREEZE experiment henceforth) composed of a net import of $27.5 (32.1) \times 10^3 \text{ m}^3 \text{ s}^{-1}$ in its northern and a net export of $17.0 (21.1) \times 10^3 \text{ m}^3 \text{ s}^{-1}$ in its southern part (Fig. 12). Net import is equivalent to net melting, and 25% of that imported to the northern Amundsen originates in its southern part. Net export is net production, and roughly 40% of the sea ice formed in the southern region moves northward, indicating a strong connection between the two areas, despite the zonality of the mean drift pattern (Fig. 1). Standard deviations much larger than the mean show the meridional exchange is highly variable (Fig. 12). Most sea ice imported to the northern Amundsen Sea ($30.3 (38.1) \times 10^3 \text{ m}^3 \text{ s}^{-1}$) stems from the Ross Sea, and accounts for $\approx 50\%$ of the simulated northward sea ice export ($57 \pm 15 \times 10^3 \text{ m}^3 \text{ s}^{-1}$) across 70°S between 150°W and Cape Adare (170°E). The northern Amundsen Sea is thus an important sink for the freshwater extracted by vigorous sea ice formation in the Ross Sea. For comparison, the BRIOS

northward sea ice export out of the inner Weddell Sea is $47 \pm 13 \times 10^3 \text{ m}^3 \text{ s}^{-1}$, close to the $50 \pm 18 \times 10^3 \text{ m}^3 \text{ s}^{-1}$ based on analyses of Upward Looking Sonar (ULS) measurements (Harms et al. 2001).

Model results show that sea ice exchange between the Bellingshausen and Amundsen Seas is small compared to that with the Ross Sea. In the model there is a net export of $3.0(2.0) \times 10^3 \text{ m}^3 \text{ s}^{-1}$ from the Amundsen to the Bellingshausen Sea across 100°W between the coast and the winter sea ice edge. Sea ice imported from the Bellingshausen to the southern Amundsen Sea represents 47 (76)% of the export across latter's northern boundary and 25 (32) % of the export towards the Ross Sea indicating that the Bellingshausen Sea possesses a largely independent sea ice regime from the rest of the Pacific sector. Apart from the import of Bellingshausen ice, the southern Amundsen Sea exports a total of $20.3(27.3) \times 10^3 \text{ m}^3 \text{ s}^{-1}$, 65 (70)% of which move westward into the eastern Ross Sea. There it contributes to the asymmetric Ross Sea ice production, its western sector being the main site of dense shelf water formation.

The net sea ice volume export from the southern Amundsen Sea of $17.0(21.1) \times 10^3 \text{ m}^3 \text{ s}^{-1}$ corresponds to a freshwater export of 15.5 (19.2) mSv ($1 \text{ mSv} = 1 \times 10^3 \text{ m}^3 \text{ s}^{-1}$). While less than half that of the Ross Sea continental shelf (Assmann et al. 2003), it is large enough to suggest the possibility of deep convection and shelf water formation on the smaller Amundsen shelf. Modelled winter mixed layer depths in this region do not exceed 200 m, however, and the water mass characteristics of this region (cf. Section 3.3) do not reveal the presence of dense shelf waters. The model calculates a freshwater input of 3.0 (2.0) mSv from fringing ice shelves (cf. Section 3.3). In addition, there is an atmospheric freshwater flux of 13.4 mSv according to the NCEP Reanalyses precipitation (P-E). Of the total P-E, 1.0 (1.4) mSv are exported from the southern Amundsen Sea as snow. A modelled sea ice growth rate of 0.69 (0.87) m a^{-1} , which includes thermodynamic growth and deformation, but not snow ice formation, corresponds to a freshwater extraction of 11.4 (14.3) mSv. Snow ice formation is, however, included in the model, and the difference between the growth rate and the sea ice related freshwater flux of 15.5 (19.2) mSv indicates that a further 4.1 (4.9) mSv of P-E are converted to snow ice. This leaves 8.3 (7.1) mSv of P-E freshwater input to reach the ocean surface directly. In the reference run, this freshwater input together with ice shelf basal melting balances the freshwater extracted by sea ice formation almost exactly. In T_FREEZE there is a net surface freshwater extraction of 5.8 mSv leading to artificially saline shelf waters as shown in Figure 6b. Our model indicates that 26 (25)% of the sea ice produced in the southern Amundsen Sea originates from snow ice formation, an important factor in the regional ice cover. North of 70°S , observations showed that snow ice comprised 60% of the thickness of late winter ice floes in the Amundsen sector (Jeffries et al. 1998). Nearer the coastline in the Bellingshausen Sea, a regime probably more like the southern Amundsen Sea, Jeffries et al. (1997) found 16-24

Sea ice export from the southern Amundsen into the Ross

Sea shows a bimodal cycle with one maximum in June at $22.5 \times 10^3 \text{ m}^3 \text{ s}^{-1}$ ($32.8 \times 10^3 \text{ m}^3 \text{ s}^{-1}$) and a second in September at $19.0 \times 10^3 \text{ m}^3 \text{ s}^{-1}$ ($32.8 \times 10^3 \text{ m}^3 \text{ s}^{-1}$) (Fig. 13). The June peak follows the zonal wind maximum, once the ice has thickened, while the September peak results from thick late winter ice, before the zonal wind velocity decreases in spring. For the closed ice pack between May and December the correlation between the ice export across 150°W (see Fig. 14 a for annual means) and the zonal wind velocity (see Fig. 15 a for annual means) is above 0.65, i.e., the zonal wind explains at least 45% of the transport variability, reaching a maximum of 0.89 in August. All correlation coefficients are significant at the 95% level unless mentioned otherwise. During the sea ice minimum and the onset of the growth season, from January to April, the correlation drops to 0.38 (0.32, both not significant at the 95% level) due to a looser ice pack moving less coherently, an effect possibly overestimated by the model (cf. Section 2.3).

North of the transition region the ice transport from the Ross to the Amundsen Sea (Fig. 14 b) depends equally on the sea ice extent ($r=0.77$, Fig. 4 b) and the zonal wind velocity ($r=0.68$, not shown). From May to August sea ice transports north and south of the drift transition (not shown, see Fig. 14 a & b for annual means) are anticorrelated with $r \leq -0.55$, i.e., strong westward transport south of the transition is associated with weaker eastward transport north of it and vice versa. In late winter the correlation drops for the northern part, as zonal transport there is more strongly controlled by the position of the sea ice edge.

In winter and spring, a high anticorrelation ($r \leq -0.7$ between May and December) between northward and westward sea ice transport from the southern Amundsen Sea (not shown, see Fig. 14 a & c for annual means) suggests coherent movement of the pack at large spatial scales. Events of strong southerly winds deplete the amount of sea ice that reaches the border with the Ross Sea and become a modulating factor on the zonal wind strength control on sea ice export to the Ross Sea. The drift of buoy A-3 in late 2001 was cited earlier as evidence for strong northward sea ice transport east of 150°W . The event indeed coincides with a maximum in the northward sea ice transport (Fig. 14 c), southerly winds (Fig. 15 c), and weak westward sea ice transport into the Ross Sea (Fig. 14 a) despite relatively strong easterly winds (Fig. 15 a). Model results suggest that events of strong northward sea ice transport related to southerly winds occur on several other occasions during the time period investigated, e.g. 1979 and 1989/90 (Fig. 14 c).

South of the drift transition, no statistically significant correlation exists between transports across 100°W (Fig. 14 d) and 150°W (Fig. 14 a), even though various features can be identified in both time series and transport across 100°W shows a similar dependence on the zonal winds as that across 150°W . The interdependence between transport south (Fig. 14 d) and north (Fig. 14 e) of the transition is considerably stronger for 100°W than for 150°W . Spanning only $\sim 1^\circ$ of latitude, the band of westward drift is much narrower at 100°W than at 150°W (Fig. 7) and in some years (1986, 1991, 1994 and 1999) transport on both sides

of the winter mean position of the drift transition is eastward (Fig. 14 d & e). With the high variability at 100°W , the reverse situation also occurs, e.g. in 1998, when transports both north and south of the transition were westward (Fig. 14d,e).

Between 1978 and 2001, a strong increase in sea ice volume south of the transition region ($1.97 \times 10^{10} \text{ m}^3 \text{ a}^{-1}$ reference, $2.55 \times 10^{10} \text{ m}^3 \text{ a}^{-1}$ T_FREEZE, Fig. 15 b) is connected to a negative trend in NCEP meridional wind velocity (0.026 m s^{-1} per year, Fig. 15 c). All trends are statistically significant at the 95% level unless stated otherwise. Since the decrease in drift velocity is compensated by an increase in the mean sea ice thickness, no significant decrease in the northward sea ice transport occurs (Fig. 14 c).

Beginning in 1981 the reference experiment shows an increase of 0.48 mSv per year of the annual mean surface freshwater flux with years of net freshwater addition starting in the early 1990s (Fig. 16 a). The ice shelf freshwater flux shows no significant trend (Fig. 16 b), but was higher during the 1990s because of the positive anomaly in deep ocean temperatures during this period (Assmann and Timmermann 2005). A weak increase appears in the annual mean P-E (0.08 mSv per year, Fig. 16 b), but is only significant from November to February (not shown, $0.10\text{-}0.27 \text{ mSv a}^{-1}$). Precipitation during these months more likely reaches the ocean surface directly, rather than being exported as snow or converted to snow ice, thus contributing to the increase in the surface fresh water flux. The striking positive anomaly in 1980 in the surface freshwater flux (Fig. 16 a & c) corresponds to a similarly extreme maximum in the NCEP air temperatures (Fig. 15 d) which induced weak April sea ice growth and strong December melting. The event corresponds to the absolute minimum in sea ice extent (Fig. 4 b) and in ice volume south of the transition region (Fig. 15 b) during the 1978-2001 period.

The annual mean freshwater flux due to sea ice growth in the reference experiment increases by 0.16 mSv a^{-1} (Fig. 16 c), not a significant trend, but significant decreases in sea ice growth occur in some months (1.6 mSv a^{-1} in April, 0.73 mSv a^{-1} in June and 0.95 mSv a^{-1} in August), with similar trends in T_FREEZE. These signals are caused in part by the upwelling of anomalously warm ocean deep waters (Assmann and Timmermann 2005) under a thicker sea ice cover (Fig. 15 b), rather than simply an increase in air temperatures (Fig. 15 d).

6. Conclusions

The drift of buoys deployed on the relatively unknown pack ice in the Amundsen Sea and monitored for up to 580 days has helped to evaluate the performance of a circumpolar coupled sea ice-ocean model in the southeast Pacific sector of the Southern Ocean. Comparisons between model results, buoy data, NCEP winds, and sea ice and ocean observations have facilitated this study of sea ice production, drift, and interannual variability. The simulated sea ice extent and drift are consistent with satellite data, and modelled winter ice thicknesses are realistic. Overly warm NCEP summer air temperatures result in an underestimate

of the summer ice cover, which can be remedied by restricting model air temperatures over the ice to values below the surface freezing point. This also leads to a thicker and more rigid ice cover, improving the modelled sea ice drift on small spatial and temporal scales. It leads to an unrealistic formation of saline shelf waters, however, in turn suggesting that freshwater input to the shelf region is underestimated.

A transition region characterized by highly variable drift velocities separates a zone of slow westward drift within ~ 200 km of the coast, driven mainly by easterlies, from a broad northern band of faster eastward drift, driven by westerlies and the ACC. The model reproduces drift events at scales approaching its resolution, but is unable to do so with shorter, small-scale events due to localised high wind speeds. Extensive comparisons in the literature and our short comparison indicate that NCEP wind speeds are generally too slow and do not capture peak speeds during events of strong winds. Also, the transition between easterly and westerly winds is slightly displaced in the coarsely resolved NCEP reanalyses. Consequently, representation of sea ice drift in the transition region is less accurate than that of the westward coastal drift where the simulated matches the observed drift closely.

Model sensitivity studies confirm that wind is the dominant driving force of the sea ice drift. The influence of ocean surface currents is only detectable in the transition region, where no definite drift direction is imposed by the winds. Sea ice drift speeds are similar for all three buoy tracks, i.e., in the coastal westward drift and in the transition region, despite very different velocity components. A comparison of modelled and observed drift velocities with the NCEP winds suggests that the free drift assumption approximately applies to the Amundsen Sea. Sea ice drift thus does not appear to be strongly convergent, so that ice thickness increases by deformation are limited. While dynamic processes contribute to the formation of the thick ice pack, they are probably not its main formation mechanism.

South of the drift transition, model results show that ≈ 65 % of the sea ice formed in the Amundsen Sea is exported to the eastern Ross Sea, where it will reduce ice growth and contribute to the strong east-west gradient in ice formation and shelf water salinity. North of the transition region the Amundsen forms a sink for half the sea ice exported from the Ross Sea. Our results indicate that for the Amundsen Sea a much higher degree of exchange occurs with the Ross to the west than with the Bellingshausen Sea to the east, which thus appears to harbor a relatively independent sea ice regime. While the average drift is zonal, events of strong northward transport occur regularly. In addition to that confirmed by the drift of buoy A-3 in 2001 there are several events of strong northward transport earlier in the time period investigated. These coincide with strong southerlies which can persist for several weeks or months as seen in the comparison of ship and NCEP winds for February and March 2000. Sea ice transport across the transition is thus highly variable. Strong northward sea ice transport may deplete the sea ice available for export to the Ross Sea, thereby representing a second control factor on the latter in addition

to the zonal wind strength.

An increase in sea ice volume over the time period investigated correlates positively with a decrease of the meridional wind strength. Northward sea ice transport does not show a similar decline since the decrease in drift velocities is compensated by an increase in ice thickness. Sea ice growth rates show a decrease in winter due to increased heat supply caused by the presence of a positive temperature anomaly within the shelf break current (Assmann and Timmermann 2005) under a thicker sea ice cover. In the reference experiment this trend is increased further by stronger November melting due to warmer air temperatures.

In the southern Amundsen, the amount of freshwater added by precipitation (P-E) is similar to that extracted by sea ice formation, playing a more important role in the surface freshwater balance here than on the Ross Sea continental shelf. Only a small part of that precipitation is exported as snow, but model and observations show that snow ice constitutes $\sim 25\%$ of the sea ice volume, increasing the ice thickness beyond that attainable by thermodynamic growth. In addition, precipitation that reaches the ocean surface helps to stabilise the upper water column, thereby damping deep convection and lengthening the life of thick ice (Marshall and Wolff 2001). Our results thus place great importance on the quality of precipitation data for the area. However, while precipitation is believed to be high in the Amundsen Sea (King and Turner 1997), more reliable and extensive data would be desirable to more accurately assess its role in the freshwater budget.

In our model, the freshwater flux due to ice shelf basal melting is $\sim 20\%$ of that from precipitation. Though the strong melting of the region's smaller ice shelves (Jacobs et al. 1996, Jenkins et al. 1997) is neglected due to model resolution, this freshwater input still makes the total surface freshwater budget of the Amundsen Sea near-neutral. Basal melting might therefore play an important role in the freshwater budget of the southern Amundsen Sea, possibly in offsetting higher brine release as suggested by our T_FREEZE experiment. Additional observations and modelling of the area at higher resolution is necessary to obtain a more accurate view on the ice shelves' role in the region's freshwater budget.

Observations (Jacobs et al. 2002) and model results (Assmann and Timmermann 2005) indicate the Amundsen Sea as the upstream region of origin for variations in the shelf water salinities in the Ross Sea. Both find a freshening in the sub-surface waters entering the Ross Sea continental shelf which are formed in the southern Amundsen Sea. Our results of a positive trend in the surface freshwater fluxes for the reference experiment, and, more importantly, of a change from a net fresh water extraction to an addition in the 1990s due to increased precipitation and decreased sea ice formation gives support to this hypothesis. They also illustrate the sensitivity of the surface freshwater balance of the southern Amundsen Sea on any of its three components - sea ice, precipitation and ice shelves.

Acknowledgments. Special thanks to Ralph Timmermann

for the use of his model code and patient assistance and to Lutz Sellmann for pre-processing the buoy data. Tina Tin and Martin Jeffries provided sea ice thickness data, and Phil Mele the RVIB *N.B. Palmer* winds. We would like to thank Ron Kwok and anonymous reviewers for helpful and detailed reviews that helped to improve the manuscript. The NCEP atmospheric forcing fields were received via the NOAA-CIRES Climate Diagnostics Centre, Boulder, Colorado (<http://www.cdc.noaa.gov/>). Support for this work was provided in part by grants from NSF/OPP. Lamont-Doherty Earth Observatory contribution LDEO #6753.

References

- Assmann, K., H.H. Hellmer, and A. Beckmann (2003), Seasonal variation in circulation and water mass distribution on the Ross Sea continental shelf. *Ant. Sci.*, **15**(1), 3-11, DOI:10.1017/S0954102003001007.
- Assmann, K.M., and R. Timmermann (2005), Variability of dense water formation in the Ross Sea. *Ocean Dynamics*, in press.
- Comiso, J. (1999, updated 2002), Bootstrap sea ice concentrations for NIMBUS-7 SMMR and DMSP SSM/I. Boulder, CO, USA: National Snow and Ice Data Center, Digital media. [Available online at <http://nsidc.org/data/nsidc-0079.html>.]
- Cullather, R.I., D.H. Bromwich, and R.W. Grumbine (1997), Validation of operational numerical analyses in Antarctic latitudes. *J. Geophys. Res.*, **102**(D12), 13,761-13,784.
- Drinkwater, M.R., X. Liu, J. Maslanik, and C. Fowler (1999), Optimal analysis products combining buoy trajectories and satellite-derived ice-drift field. In *IPAB Biennial Meeting Report*, May 11-13, 1998, Naples, Italy, WCRP Rep. 5/1999, 1-11, World Climate Research Program, Geneva.
- Fischer, H. (1995), Vergleichende Untersuchungen eines optimierten dynamisch - thermodynamischen Meereismodells mit Beobachtungen im Weddellmeer [Comparison of an optimized dynamic - thermodynamic sea ice model with observations in the Weddell Sea.]. *Berichte zur Polarforschung*, **166**, 130 pp., Alfred-Wegener-Institute, Bremerhaven.
- Giulivi, C.F., and S.S. Jacobs (1997), Oceanographic Data in the Amundsen and Bellingshausen Seas, NB Palmer Cruise 9402, Feb-Mar 1994. Tech. Rept. LDEO-97-3, 330 pp., Lamont-Doherty Earth Observatory of Columbia University, Palisades.
- Gloersen, P., W.J. Campbell, D.J. Cavalieri, J.C. Comiso, C.L. Parkinson, and H.J. Zwally (1992), Arctic and Antarctic sea ice : Satellite passive-microwave observations and analysis. 290 pp., National Aeronautics and Space Administration (NASA), Washington, DC.
- Gouretski, V., and K. Jancke (1998), A New World Ocean Climatology: Objective Analysis on Neutral Surfaces. WHP Special Analysis Centre. Technical Report No. 3, 12 pp., 27 Plates, Hamburg.

- Greischar, L.L., C.R. Bentley, and L.R. Whiting (1992), An analysis of gravity measurements on the Ross Ice Shelf, Antarctica. *Ant. Res. Ser.*, **57**, 105-155.
- Haidvogel, D.B., J.L. Wilkin, and R.E. Young (1991), A semi-spectral primitive equation ocean circulation model using vertical sigma and orthogonal curvilinear horizontal coordinates. *J. Comp. Phys.*, **94**, 151-185.
- Harms, S., E. Fahrback, and V.H. Strass (2001), Sea ice transports in the Weddell Sea. *J. Geophys. Res.*, **106(C5)**, 9057-9073.
- Hellmer, H.H., S.S. Jacobs, and A. Jenkins (1998), Oceanic erosion of a floating Antarctic glacier in the Amundsen Sea. *Antarct. Res. Ser.*, **75**, 83-99.
- Hellmer, H.H. (2004), Impact of Antarctic ice shelf basal melting on sea ice and deep ocean properties. *Geophys. Res. Lett.*, **31**, 10.1029/2004GL019506.
- Hibler, W.D., III (1979), A dynamic-thermodynamic sea ice model. *J. Phys. Oceanogr.*, **9(4)**, 815-846.
- Jacobs, S.S., H.H. Hellmer, and A. Jenkins (1996), Antarctic ice sheet melting in the Southeast Pacific. *Geophys. Res. Lett.*, **23**, 957-960.
- Jacobs, S.S., and J.C. Comiso (1997), Climate variability in the Amundsen and Bellingshausen Sea. *J. Clim.*, **10**, 697-709.
- Jacobs, S.S., C.F. Giulivi, and P.A. Mele (2002), Freshening of the Ross Sea during the late 20th century, *Science*, **297**, 386-389.
- Jeffries, M.O., A.P. Worby, K. Morris, and W.F. Weeks (1997), Seasonal variations in the properties and structural composition of sea ice and snow cover in the Bellingshausen and Amundsen Seas. *J. Glaciol.*, **43**, 138-151.
- Jeffries, M.O., S. Li, R.A. Jana, H.R. Krause, and B. Hurst-Cushing (1998), Late winter first-year ice floe variability, seawater flooding and snow ice formation in the Amundsen and Ross Seas. *Ant. Res. Ser.*, **74**, 69-88.
- Jenkins, A., D.G. Vaughan, S.S. Jacobs, H.H. Hellmer, and J.R. Keys (1997), Glaciological and oceanographic evidence of high melt rates beneath Pine Island Glacier, West Antarctica. *J. Glaciol.*, **43**, 114-121.
- Jones, A.G.E. (1982), Antarctica Observed, Caedmon of Whitby, Yorkshire.
- King, J.C., and J. Turner (1997), Antarctic Meteorology and Climatology, 409pp., Cambridge University Press, Cambridge.
- Kottmeier, C., and J. Lüdemann (1996), Meereisbojen 1986-1995: Technische Dokumentation, Berichte aus dem Fachbereich Physik, 69, 73 pp., Alfred Wegener Institute, Bremerhaven.
- Lecointe, G. (1904), Au pays des Manchots, Bruxelles.
- Leppäranta, M. (1983) A growth model for black ice, snow ice, and snow thickness in subantarctic basins. *Nordic Hydrology*, **14**, 59-70.
- Marsland, S.J., and J.-O. Wolff (2001), On the sensitivity of Southern Ocean sea ice to the surface fresh water flux: A model study. *J. Geophys. Res.*, **106(C2)**, 2723-2741.

- Martinson, D.G., and C. Wamser (1990), Ice drift and momentum exchange in winter Antarctic pack ice. *J. Geophys. Res.*, **95(C2)**, 1741-1755.
- Owens, W.B. and P. Lemke (1990), Sensitivity studies with a sea ice-mixed layer-pycnocline model in the Weddell Sea. *J. Geophys. Res.*, **95(C6)**, 9527-9538.
- Parkinson, C.L., and W.M. Washington (1979), A large-scale numerical model of sea ice. *J. Geophys. Res.*, **84(C1)**, 311-337.
- Philbrick, N. (2003), *Sea of Glory*, Viking, New York.
- Semtner, A.J., Jr. (1976), A model for the thermodynamic growth of sea ice in numerical investigations of climate. *J. Phys. Oceanogr.*, **6(3)**, 379-389.
- Smith, S.R., D.M. Legler, and K.V. Verzone (2001), Quantifying uncertainties in NCEP Reanalyses using high-quality research vessel data, *J. Clim.*, **14(20)**, 4062-4072.
- Smith, W.H.F., and D.T. Sandwell (1997), Global Sea Floor Topography from Satellite Altimetry and Ship Depth Soundings. *Science*, **277**, 1956-1962.
- Tennant, W. (2004), Considerations when using pre-1979 NCEP/NCAR reanalyses in the southern hemisphere. *Geophys. Res. Lett.*, **31**, 10.1029/2004GL019751.
- Timmermann, R., A. Beckmann, and H.H. Hellmer (2002 a), Simulation of ice-ocean dynamics in the Weddell Sea. Part I: Model configuration and validation. *J. Geophys. Res.*, **107(C3)**, doi: 10.1029/2000JC000471.
- Timmermann, R., H.H. Hellmer, and A. Beckmann (2002 b), Simulation of ice-ocean dynamics in the Weddell Sea. Part II: Interannual variability 1985-1993. *J. Geophys. Res.*, **107(C3)**, doi: 10.1029/2000JC000472.
- Worby, A.P. and I. Allison (1999), A technique for making ship-based observations of Antarctic sea ice thickness and Characteristics, Part 1: Observational Technique and Results. ASPeCt Report No. 14, Antarctic CRC, Hobart.
- Yuan, X., and D.G. Martinson (2000), Antarctic sea ice extent and its global connectivity, *J. Clim.*, **13**, 1697-1717.
- Yuan, X. (2004), High-wind speed evaluation in the Southern Ocean. *J. Geophys. Res.*, **107**, D13101, doi: 10.1029/2003JD004179.

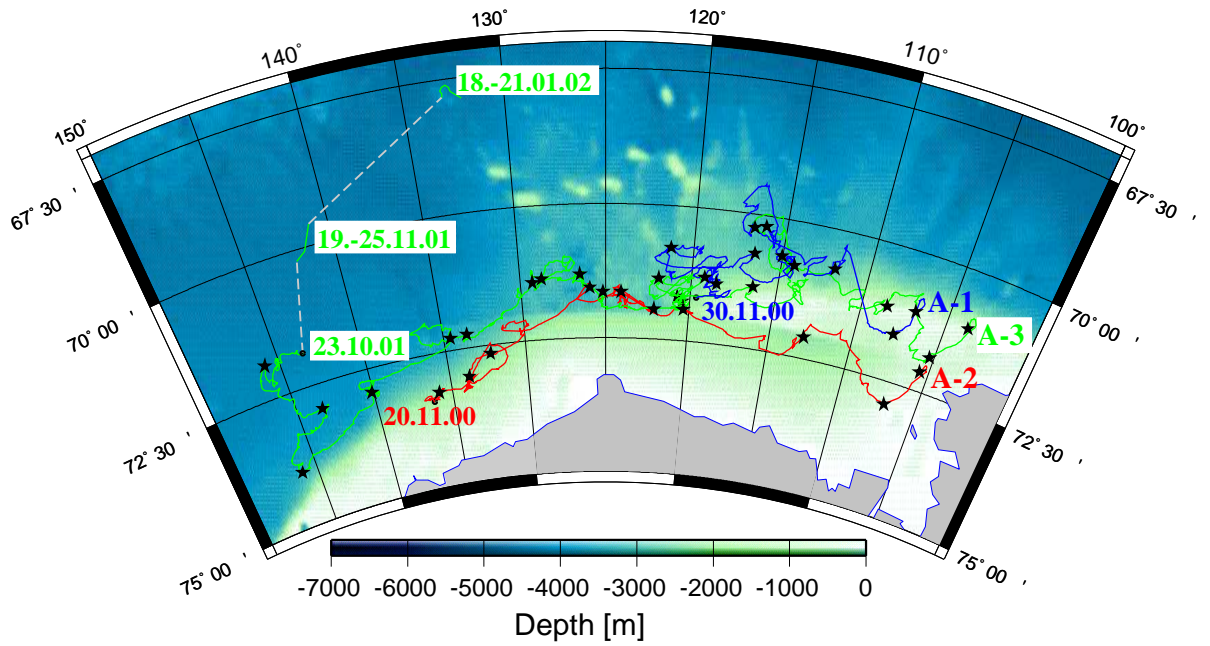


Figure 1. Bottom topography (ETOPO 2; available at www.ngdc.noaa.gov/mgg/global) and drift tracks of AWI buoys A-1 (blue), A-2 (red), and A-3 (green). Stars indicate the beginning of a new month. Dates mark the end of periods of continuous data transmission (colored solid lines).

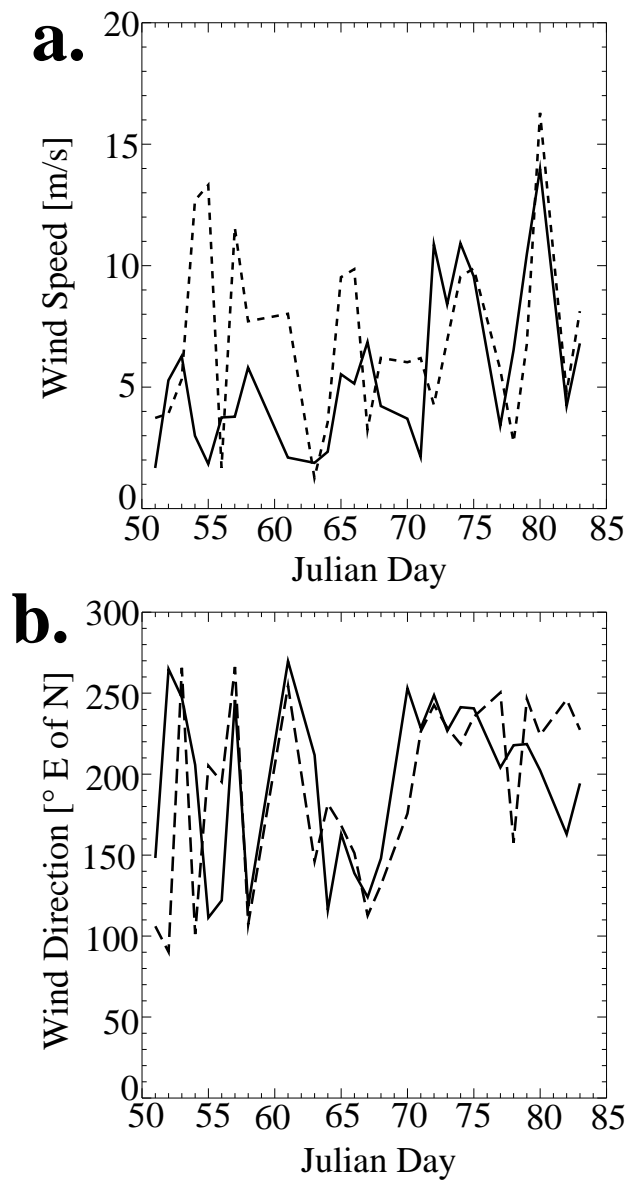


Figure 2. Comparison of daily mean magnitude (a) and direction (b) of NCEP 10-m winds (solid lines) and observed winds on cruise NBP00-01 (dashed lines) mostly over the continental shelf and slope from 150° W (20 Feb 2000) to 104° W (23 Mar 2000).

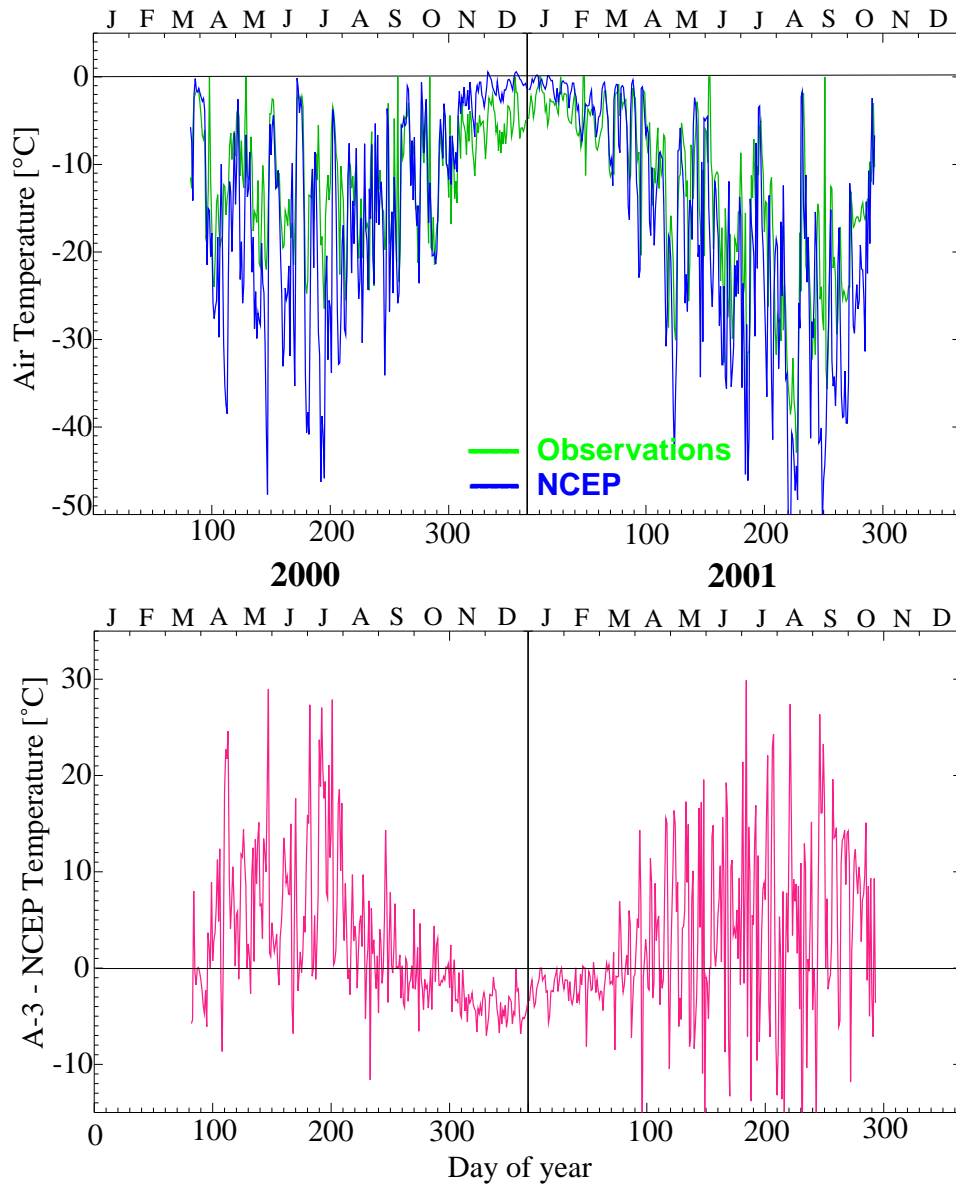


Figure 3. Daily average observed air temperatures (green) and NCEP values at the nearest model grid point (blue) along with their difference (lower panel) along the track of buoy A-3. The buoy temperatures are accurate to 0.3°C (Kottmeier & Lüdemann 1996). The correlation between the observed and NCEP air temperatures is $r=0.77$, is significant at the 95% level based on a two-sided Student's t-test.

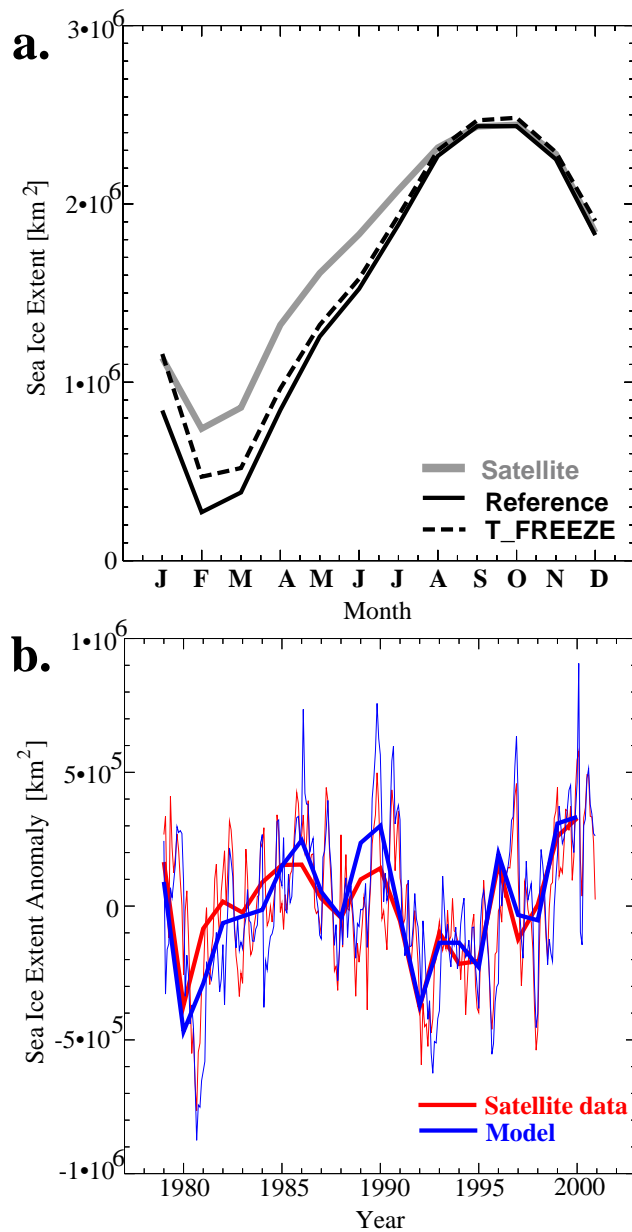


Figure 4. For the Amundsen Sea ($100^\circ\text{W} - 150^\circ\text{W}$): **a.** Mean annual cycle (1979-2000) of monthly mean simulated (black) and satellite (gray) sea ice extent. **b.** Sea ice extent anomalies in the Amundsen Sea as represented in the model reference simulation (blue, annual means thick line, monthly means thin line) and in the satellite data (red). Sea ice extent is defined as the area over which sea ice concentration exceeds 15%.

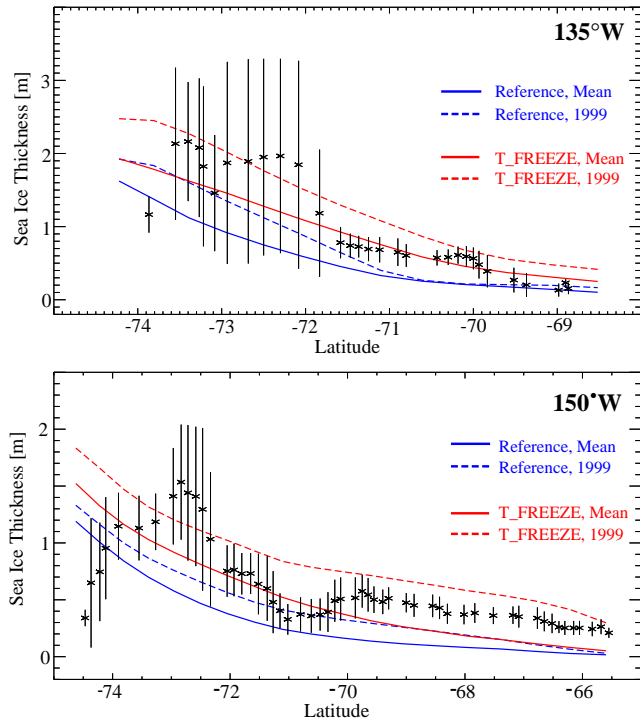


Figure 5. Sea ice thickness for January along 135°W and 150°W. The 1999 observations (crosses), essentially snapshots over an area of approximately 1 km² (Worby & Allison 1999) every 16 km along track, were smoothed with a three-point running mean to make the scale of variation comparable to the 50×50 km model resolution in this region. Error bars on the observations represent the combined error of the spread of values associated with smoothing and a 15 % error inherent in the measurement technique (Worby & Allison 1999).

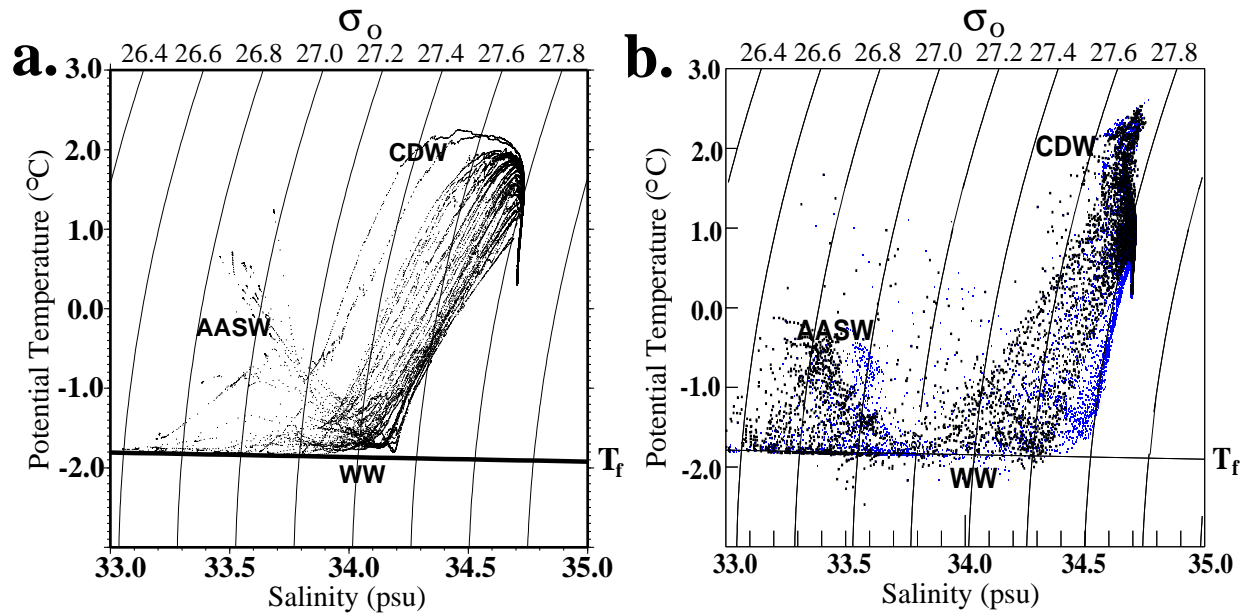


Figure 6. θ/S diagrams for the Amundsen Sea (100°W to 150°W , South of 67°S). a. Observations taken in March 1994 during *Nathaniel B. Palmer* cruise NBP94-02 (Giulivi and Jacobs 1997). b. Modelled mean for March 1994 for the reference (black) and T_FREEZE (blue) experiments. The diagrams are supplemented by isopycnals (σ_0) and surface freezing temperature (T_f). ASSW: Antarctic Surface Water. WW: Winter Water. CDW: Circumpolar Deep Water.

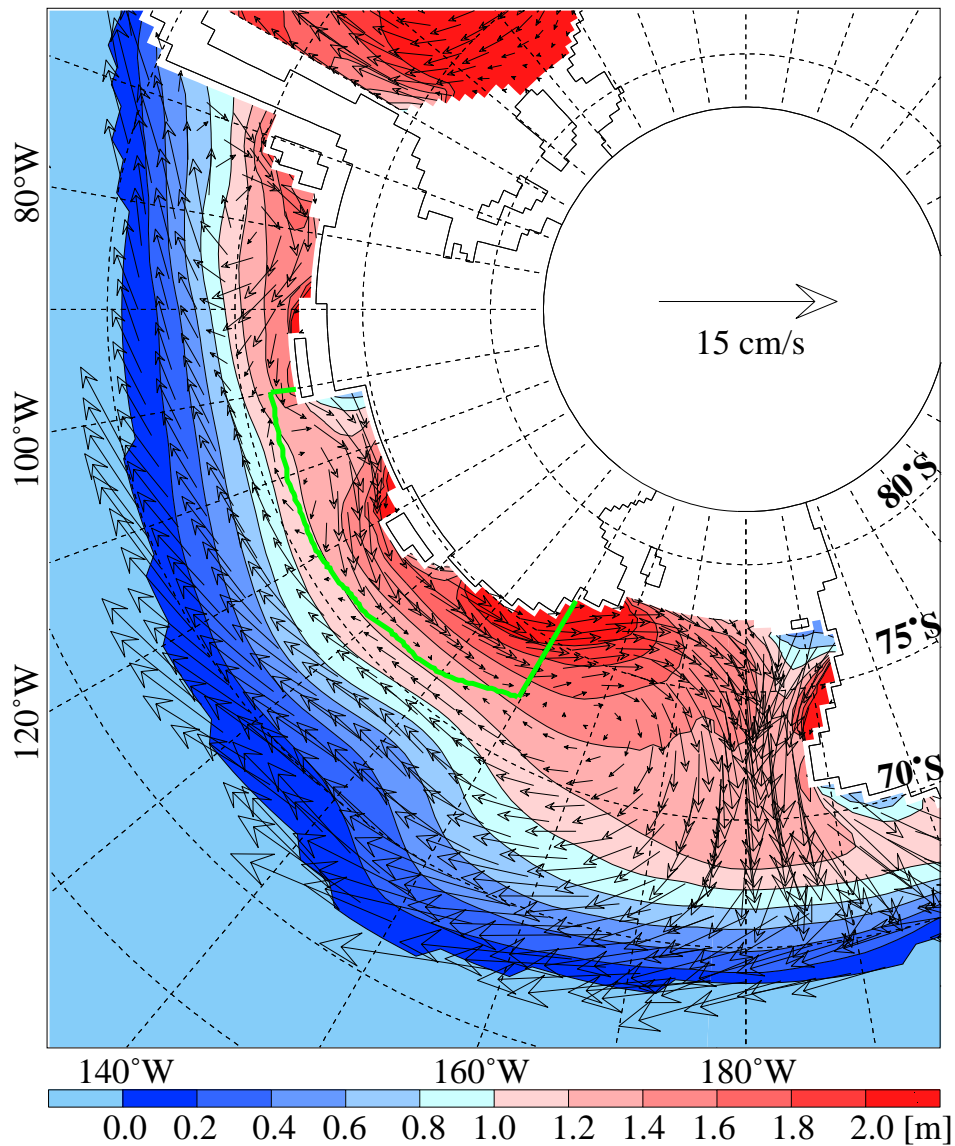


Figure 7. Winter (May-October) mean (1978-2001) modelled sea ice drift velocities (vectors) and thickness (colour-coded). Vectors are shown for every fourth model grid point, i.e., every second one zonally and meridionally. The winter mean position of the transition from eastward to westward drift in the Amundsen Sea is marked by the zonal part of the green line, while its meridional parts mark the eastern and western boundaries of the Amundsen Sea.

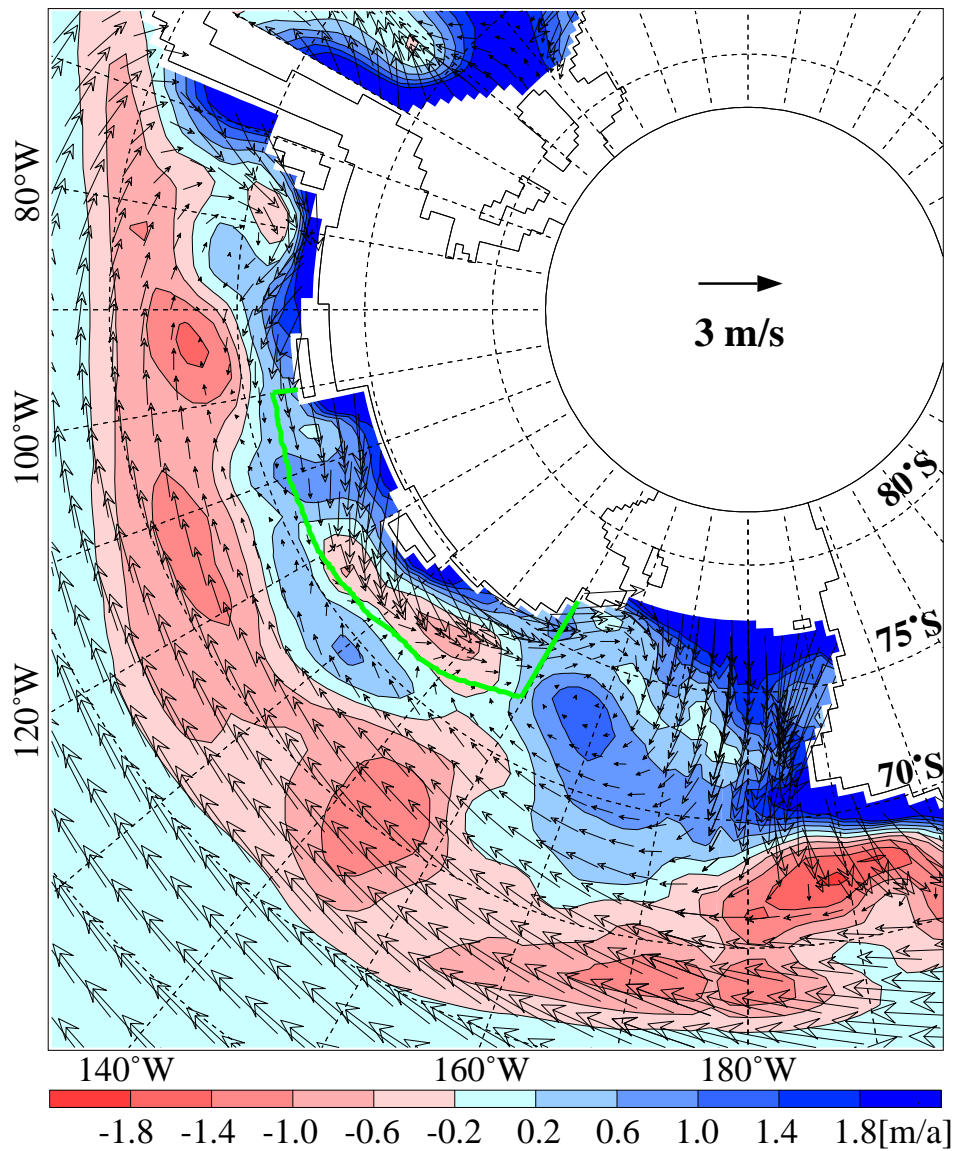


Figure 8. Modelled mean (1978-2001) net annual sea ice growth rate in the Pacific sector (colour-coded) and winter (May-October) mean (1978-2001) NCEP 10-m wind velocities. Negative freezing rates denote melting. Wind vectors and green lines as in Fig. 7.

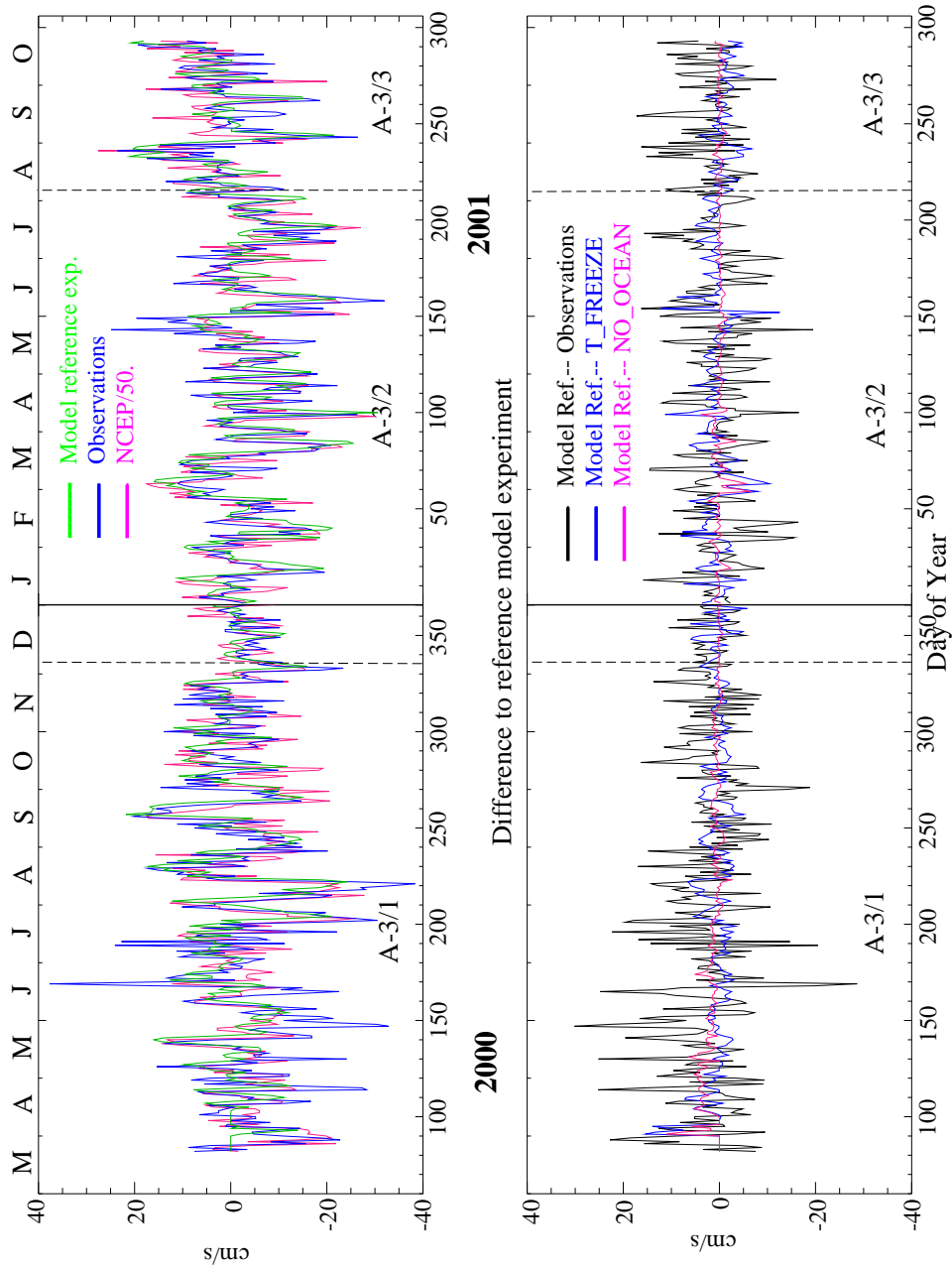
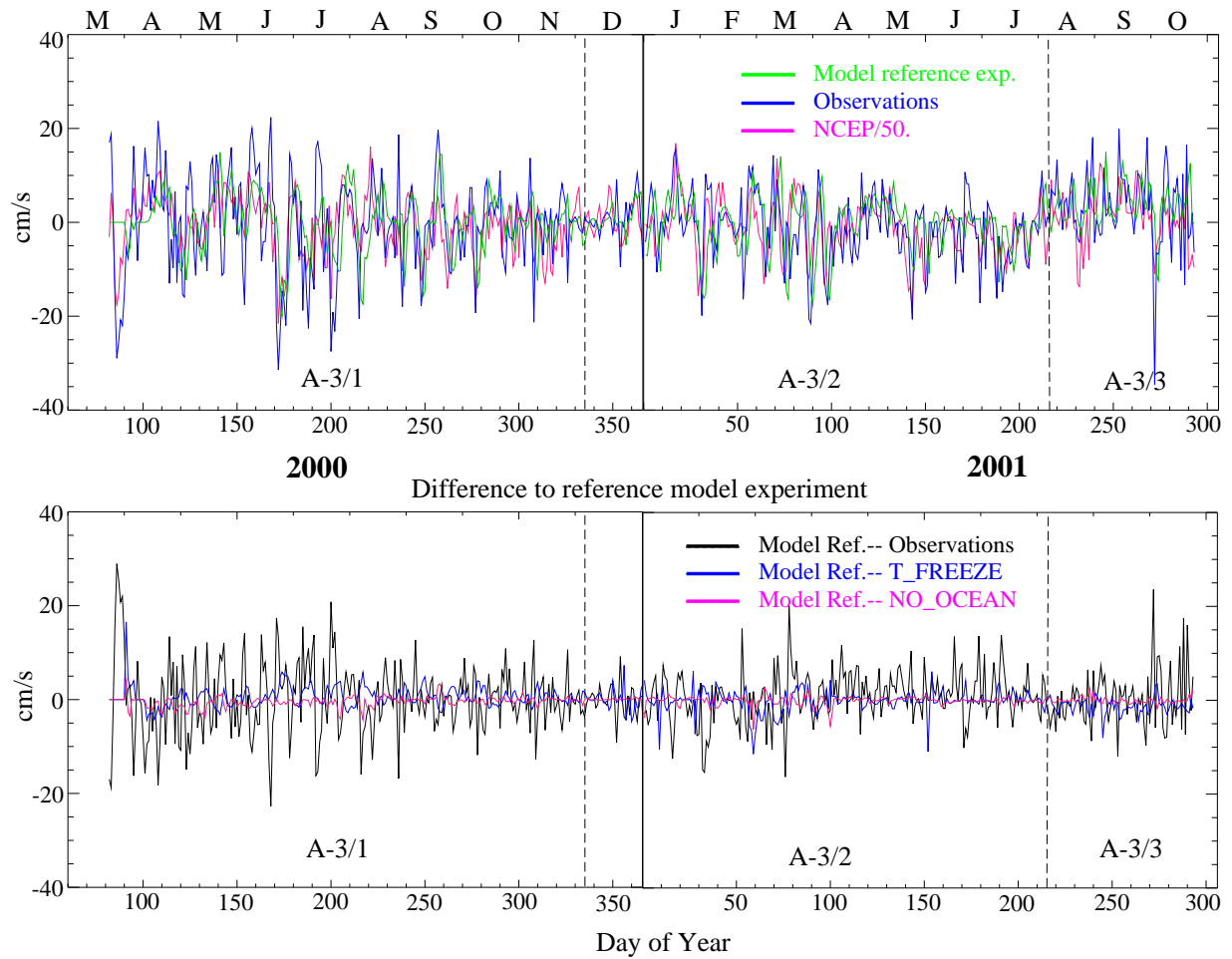


Figure 9. Top panel: Time series of observed (blue) and simulated (green) daily average zonal sea ice drift velocity component and NCEP zonal wind velocities (magenta) along the track of buoy A-3. Bottom panel: Difference in zonal velocity of the reference simulation and the observations (black), the T_FREEZE sensitivity experiment (blue), and the NO_OCEAN sensitivity experiment (magenta) (lower panel). NCEP wind velocities were divided by 50 to make them comparable in scale to the sea ice drift velocities.

Figure 10. As in Fig. 9, but for meridional velocity.



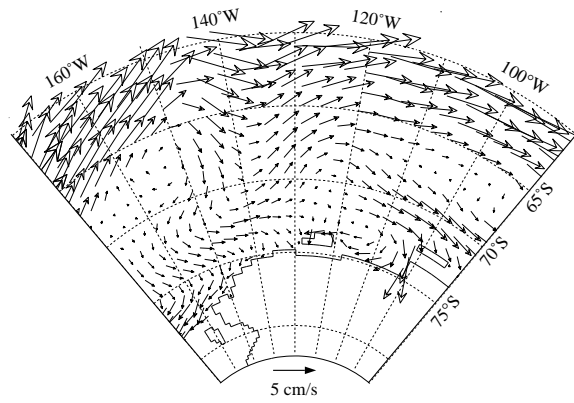


Figure 11. Mean (1978-2001) modelled ocean surface currents. Vectors are shown for every fourth model grid point for better visibility.

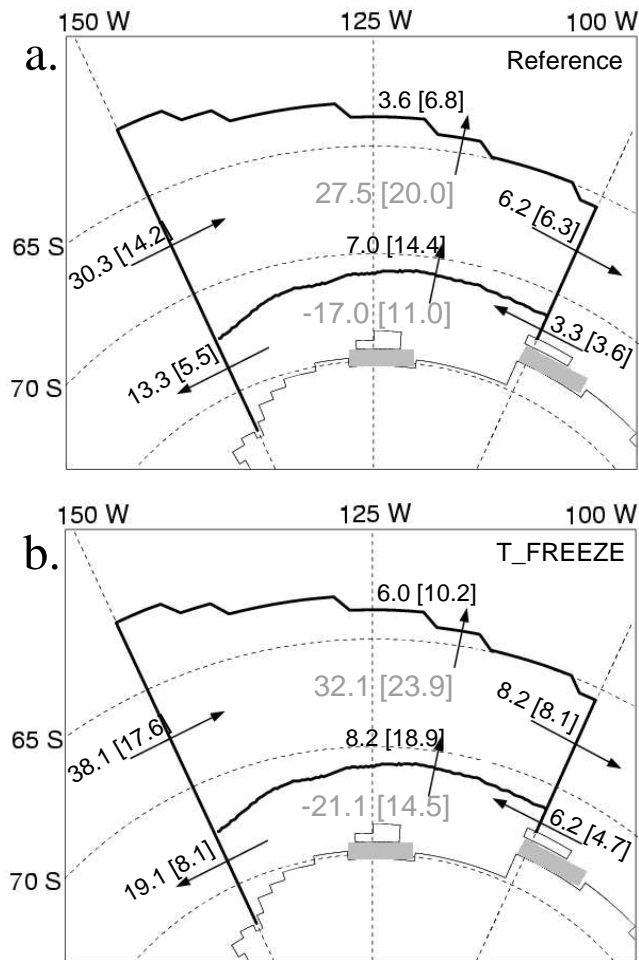


Figure 12. Schematic diagram of mean (1978-2001) annual sea ice transport across the boundaries of the Amundsen Sea for **a.** the reference and **b.** T_FREEZE model experiments. Ice shelves as represented in the model are shaded gray. Net transports from the southern and northern Amundsen Sea are given in gray with net import defined as positive. Standard deviations (in square brackets) are for range of annual mean transports. Units are in $10^3 \text{ m}^3 \text{ s}^{-1}$.

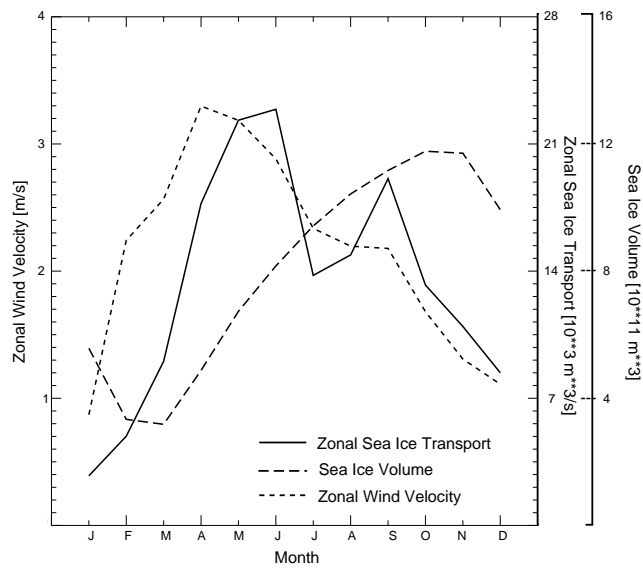


Figure 13. Mean annual cycle (1978-2001) of monthly mean zonal sea ice transport across 150°W south of the winter mean position of the drift transition (solid line, right scale), zonal wind velocity (dotted line, left scale), and sea ice volume south of the winter mean drift transition (dashed line, far right scale). For an easier comparison with the ice volume westward transport and velocity are defined as positive in this figure.

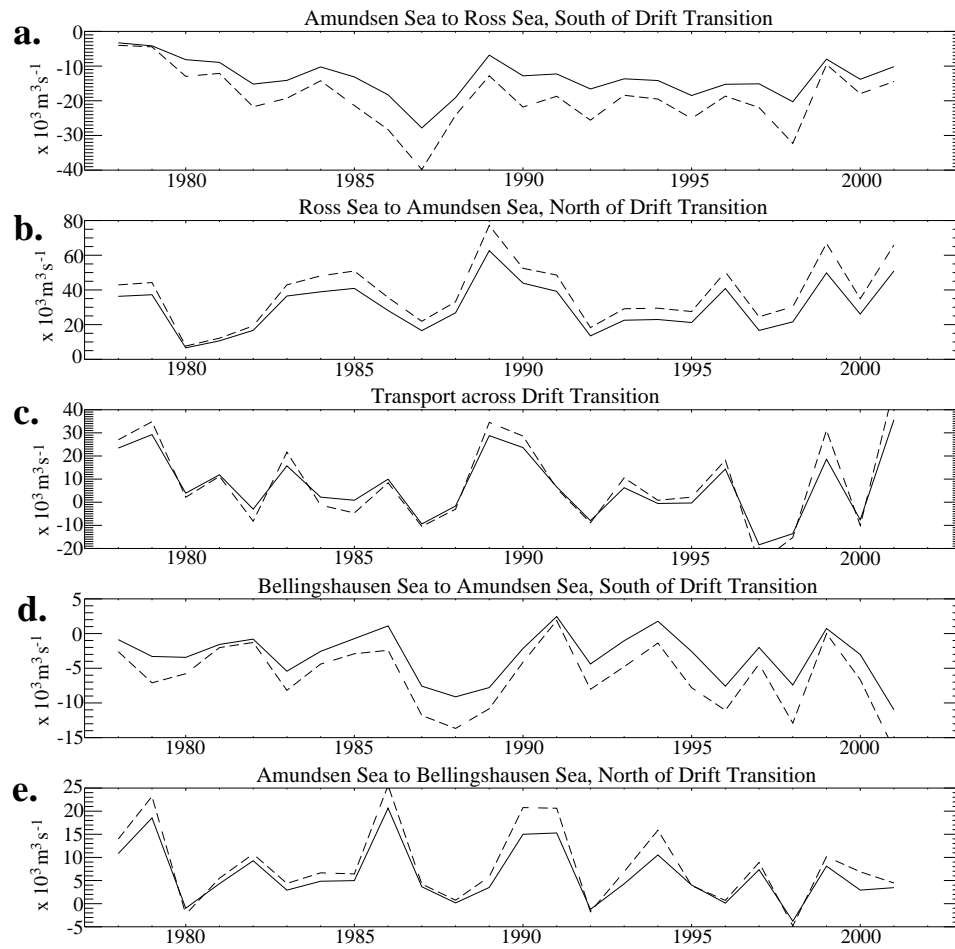


Figure 14. Time series of annual mean sea ice transports for the Amundsen Sea sector for the reference (solid) and T_FREEZE (dashed) experiments : **a.** across 150°W south of the transition region, **b.** across 150°W north of the transition region, **c.** across the transition region, **d.** across 100°W south of the transition region, **e.** across 100°W north of the transition region. Eastward and northward transports are defined as positive.

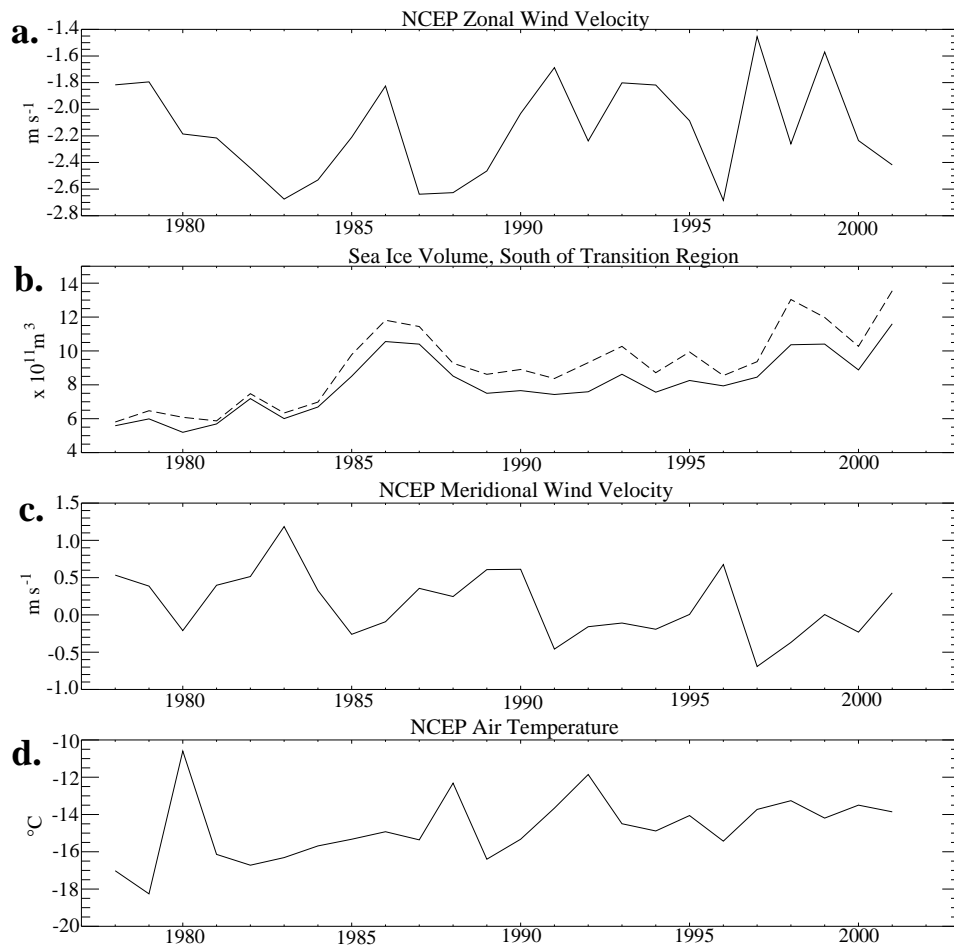


Figure 15. For the Amundsen Sea (100°W - 150°W, south of the transition region) annual means of: **a.** NCEP zonal wind velocity, **b.** Sea ice volume for the reference (solid) and T_FREEZE (dashed) experiments, **c.** NCEP meridional wind velocity, **d.** NCEP air temperatures. Eastward and northward velocities are defined as positive.

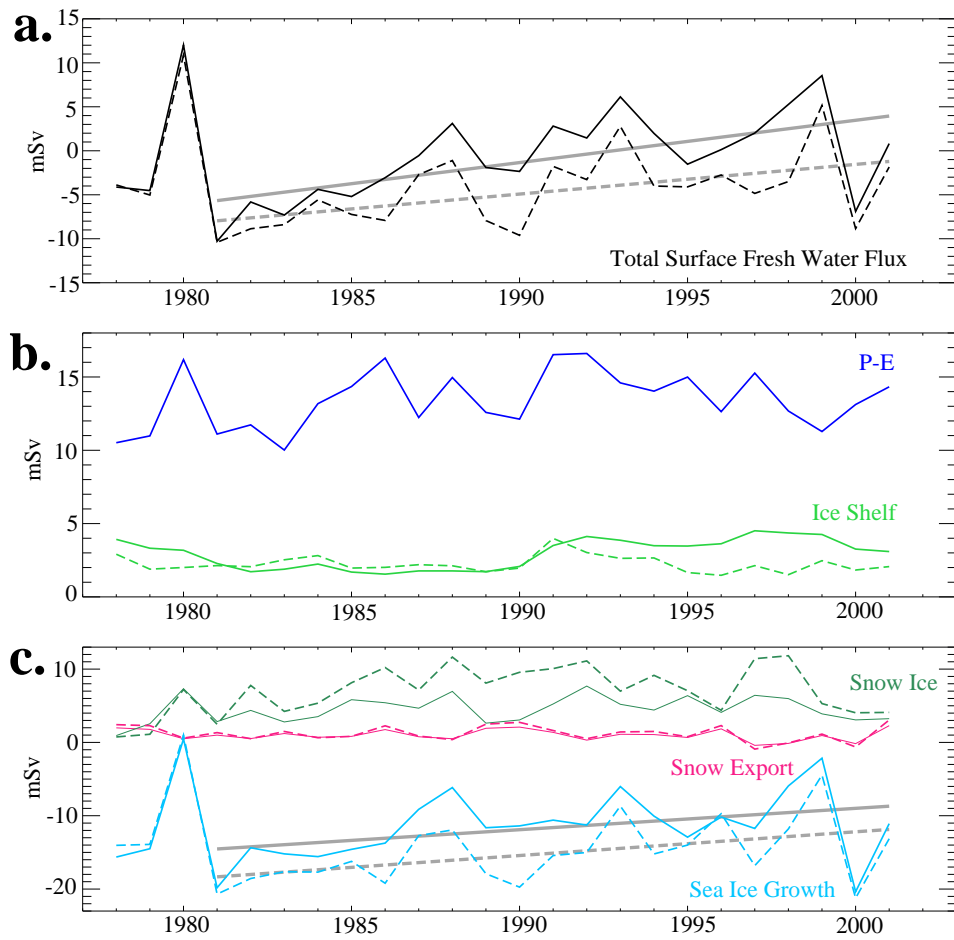


Figure 16. For the Amundsen Sea ($100^{\circ}\text{W} - 150^{\circ}\text{W}$, south of the transition region), annual means for the reference (solid) and T_FREEZE (dashed) experiments, all as fresh-water fluxes in mSv ($1 \text{ mSv} = 10^3 \text{ m}^3 \text{ s}^{-1}$): **a.** total surface fresh-water flux, fresh water fluxes due to **b.** NCEP precipitation P-E (blue) and ice shelf basal melting (green), **c.** sea ice growth (blue), snow export (red) and snow ice formation (dark green). Gray lines in panels **a.** and **c.** represent the trends in the time series from 1981 to 2001.

Table 1. Drift details of AWI buoys A-1, A-2, and A-3. Date and position are provided for start and end of the drift, which defines the duration. Interrupted data transmissions reduced the actual number of days with observations to 207 (A-1), 232 (A-2) and 568 (A-3). Distances given are cumulative travel distances from point to point. The last three columns contain the mean speed and mean zonal and meridional velocity components for each buoy. Analysis of the drift of A-3 was split into three parts (Fig. 1): A-3/1 encompassing the early drift similar to A-1, A-3/2 the quasi-zonal drift thereafter, and A-3/3 the northward drift. Eastward and northward velocities are defined as positive.

ID	Date	Position	Duration [day]	Distance [km]	Speed [cm/s]	u_{mean} [cm/s]	v_{mean} [cm/s]
A-1	20 Mar 00	71.09°S; 106.89°W	252	3320	14.5	-2.0	-0.7
	30 Nov 00	71.67°S; 119.64°W					
A-2	22 Mar 00	72.13°S; 105.56°W	242	2670	12.2	-5.0	-0.9
	20 Nov 00	73.39°S; 136.27°W					
A-3	23 Mar 00	71.08°S; 103.73°W	580	5610	11.2	-2.5	-0.1
	23 Oct 01	71.87°S; 143.50°W					
A-3/1	23 Mar 00	71.08°S; 103.73°W	253	2850	13.1	-2.8	-0.3
	30 Nov 00	71.91°S; 121.50°W					
A-3/2	01 Dec 00	71.93°S; 122.11°W	243	2100	10.0	-3.7	-1.0
	31 Jul 01	73.96°S; 145.62°W					
A-3/3	01 Aug 01	73.96°S; 146.16°W	84	725	10.0	1.0	3.1
	23 Oct 01	71.87°S; 143.50°W					

Table 2. Mean NCEP wind velocity components and speeds and mean sea ice drift velocity components and speeds for the observed buoys and the reference and T_FREEZE model experiments along the tracks of the AWI buoys A-1, A-2, and A-3. The drift of A-3 was split as in Table 1. Eastward and northward velocities are defined as positive. Errors given are standard deviations of the daily mean values over the drift period.

ID		NCEP	Observations	Model Ref.	T_FREEZE
A-1	u[cm/s]	-94±439	-2.0±12.6	1.0±9.1	1.1 ±10.3
	v[cm/s]	-57±330	-0.7±11.0	-0.5±7.8	-1.1 ±8.6
	speed[cm/s]	489±252	14.5±8.6	9.4±5.4	11.7 ±6.8
A-2	u[cm/s]	-259±450	-5.0±10.7	-3.7±8.9	-4.7 ±10.0
	v[cm/s]	7±310	-0.9±8.0	0.6±6.1	-0.02±7.3
	speed[cm/s]	510±297	12.2±8.2	9.1±7.0	10.9 ±7.7
A-3	u[cm/s]	-113±450	-2.5±9.9	-1.0±9.1	-1.5 ±10.6
	v[cm/s]	-36±298	-0.1±8.7	0.3±6.5	0.3 ±7.4
	speed[cm/s]	471±281	11.2±7.5	9.2±6.5	10.8 ±7.2
A-3/1	u[cm/s]	-156±447	-2.8±11.3	-0.3±8.9	-0.8 ±10.3
	v[cm/s]	-47±316	-0.3±10.2	-0.2±7.0	-0.7 ±8.0
	speed[cm/s]	491±259	13.1±8.2	9.5±6.1	11.1 ±6.9
A-3/2	u[cm/s]	-184±427	-3.7±9.1	-3.4±8.6	-4.1 ±10.1
	v[cm/s]	-57±279	-1.0±6.8	-0.4±6.1	-0.3 ±6.5
	speed[cm/s]	453±301	10.0±6.5	8.8±6.7	10.2 ±7.5
A-3/3	u[cm/s]	229±402	1.0±8.5	3.4±9.3	3.9 ±10.4
	v[cm/s]	51±286	3.1±5.4	3.6±5.4	4.9 ±5.7
	speed[cm/s]	466±282	10.0±6.6	9.5±7.0	11.4 ±7.0

Table 3. Root-mean square (RMS) sea ice drift velocities for the observed buoys and the reference and T_FREEZE model experiments along the tracks of the AWI buoys A-1, A-2, and A-3. The drift of A-3 was split as in Table 1. Also shown are the correlation coefficients (r) for the observed and modelled time series of drift velocities along the buoy tracks as shown in Figs. 9 and 10 and smoothed with a 5-day running mean. All correlation coefficients are significant at the 95% level based on a two-sided Student's t-test.

ID		Observations	Model Ref.			T_FREEZE		
		RMS	RMS	r	r (5-day r.m.)	RMS	r	r (5-day r.m.)
A-1	u	12.7	9.1	0.71	0.83	9.9	0.70	0.82
	v	11.0	7.8	0.62	0.73	8.7	0.62	0.73
A-2	u	11.8	9.6	0.71	0.84	10.9	0.73	0.88
	v	8.8	6.2	0.60	0.71	7.3	0.64	0.75
A-3	u	10.3	9.2	0.71	0.82	10.5	0.70	0.82
	v	8.7	6.5	0.65	0.75	7.4	0.65	0.77
A-3/1	u	11.6	7.8	0.69	0.82	10.1	0.69	0.81
	v	10.2	6.3	0.63	0.73	8.1	0.65	0.77
A-3/2	u	9.2	8.6	0.73	0.82	10.9	0.72	0.82
	v	6.9	5.5	0.66	0.75	6.5	0.64	0.75
A-3/3	u	8.6	9.0	0.74	0.89	11.1	0.75	0.89
	v	8.6	5.7	0.66	0.81	7.4	0.62	0.79